




# Dexterous helical magnetic robot for improved endovascular access

## Journal Article

### Author(s):

[Dreyfus, Roland](#) ; [Boehler, Quentin](#) ; Lyttle, Sean; Gruber, P.; Lussi, Jonas; Chautems, Christophe; Gervasoni, Simone; Berberat, Jatta; Seibold, Dominic; Oxsenbein-Kölblle, Nicole; Reinehr, Michael; Weisskopf, Miriam; Remonda, Luca; [Nelson, Bradley](#) 

### Publication date:

2024-02

### Permanent link:

<https://doi.org/10.3929/ethz-b-000659728>

### Rights / license:

[In Copyright - Non-Commercial Use Permitted](#)

### Originally published in:

Science Robotics 9(87), <https://doi.org/10.1126/scirobotics.adh0298>

### Funding acknowledgement:

743217 - Soft Micro Robotics (EC)

185039 - Arbeitstitel "Soft Magnetic Robots: Modeling, Design and Control of Magnetically Guided Continuum Manipulators" (SNF)

952152 - MAgnetically steerable wireless Nanodevices for the tarGeted delivery of therapeutic agents in any vascular rEgion of the body (EC)

**Title:**

Dexterous helical magnetic robot for improved endovascular access

**Authors:**

R. Dreyfus<sup>1</sup>, Q. Boehler<sup>1</sup>, S. Lyttle<sup>1</sup>, P. Gruber<sup>2</sup>, J. Lussi<sup>1</sup>, C. Chautems<sup>1</sup>, S. Gervasoni<sup>1</sup>, J. Berberat<sup>2</sup>, D. Seibold<sup>1</sup>, N. Ochsenbein-Kölble<sup>3,4</sup>, M. Reinehr<sup>5</sup>, M. Weisskopf<sup>6</sup>, L. Remonda<sup>2</sup>, B. J. Nelson<sup>1\*</sup>

**Affiliations:**

<sup>1</sup>ETH Zurich, Multi-Scale Robotics Lab; Zurich, Switzerland.

<sup>2</sup>Cantonal Hospital Aarau, Department of Neuroradiology; Aarau, Switzerland.

<sup>3</sup>University Hospital Zurich, Department of Obstetrics; Zurich, Switzerland.

<sup>4</sup>University of Zurich; Zurich, Switzerland.

<sup>5</sup>University of Zurich, Institute of Pathology and Molecular Pathology; Zurich, Switzerland.

<sup>6</sup>University Hospital Zurich, University of Zurich, Center for Surgical Research, Zurich, Switzerland

\*Corresponding author. Email: bnelson@ethz.ch

**Abstract:**

Treating vascular diseases in the brain requires access to the affected region inside the body. This is usually accomplished through a minimally invasive technique that involves the use of long, thin devices, such as wires and tubes, that are manually maneuvered by a clinician within the bloodstream. By pushing, pulling, and twisting, these devices are navigated through the tortuous pathways of the blood vessels. The outcome of the procedure heavily relies on the clinician's skill and the device's ability to navigate to the affected target region in the bloodstream, which is often inhibited by tortuous blood vessels. Sharp turns require high flexibility, but this flexibility inhibits translation of proximal insertion to distal tip advancement. We present a highly dexterous, magnetically steered continuum robot that overcomes pushability limitations through rotation. A helical protrusion on the device's surface engages with the vessel wall and translates rotation to forward motion at every point of contact. An articulating magnetic tip allows for active steerability, enabling navigation from the aortic arch to millimeter-sized arteries of the brain. The effectiveness of the magnetic continuum robot has been demonstrated through successful navigation in models of the human vasculature and blood vessels of a live pig.

**One-Sentence Summary:**

Helically propelled, magnetically articulated continuum robot for tortuous vascular access.

## Main Text:

### INTRODUCTION

Among the most serious medical conditions are those that affect the blood vessels deep within the brain. These include acute ischemic stroke (AIS), where a blood clot blocks the blood flow to the brain (see Fig. 1C), and aneurysms, which can burst, leading to uncontrolled bleeding inside the brain. AIS alone is the second leading cause of death and long-term disability, affecting over 13 million people annually (1).

The treatment of these vascular diseases requires accessing the affected areas within the brain. This is usually accomplished through a minimally invasive technique that utilizes thin wires inserted into the patient's blood vessels. These devices, measuring over a meter in length, are carefully navigated by applying external manipulation, pushing, pulling, and twisting, to steer the curved tip on the other end deep within the body.

The devices are typically inserted through either the femoral artery in the leg or the radial artery in the arm and navigated towards the cerebral arteries via the aortic arch. The femoral approach is the conventional choice due to its relatively straight path from the insertion point to the arteries of the neck. The trans-radial approach has gained recognition as a feasible alternative due to the lower complication rate, but it also presents additional challenges, as it requires navigating sharp turns that are difficult to overcome using traditional devices (2).

Mechanical thrombectomy (MT) is a procedure in which the occluding blood clot is physically grasped and removed (3, 4). MT is currently the standard-of-care in large vessel occlusions in AIS patients and has increasingly replaced intra-arterial thrombolysis in which a thrombolytic agent, such as urokinase and tissue plasminogen activator (tPA), is injected in large quantities into the vessels (5, 6). MT clinical trials have helped establish it as the most effective treatment for AIS in many cases.

Although this minimally invasive endovascular treatment has revolutionized the way AIS is treated and drastically improved the patient's chance of recovery, it can be challenging for the surgeon to perform. Navigating tortuous vessels often requires multiple attempts, repeatedly stressing the vessel walls, thereby increasing the risk of vasospasm and vessel dissections (7). For example, one of the leading causes of failed reperfusion, the restoration of blood flow in occluded vessels, is the inability to reach occluded regions (8). Particularly challenging are highly tortuous vessels with sharp turns, loops, and kinks (7). In such anatomies, pushability becomes challenging because of the high friction the devices experience distally (see Fig. 1D). Too much space and a lack of proximal support cause the devices to buckle when pushed (7, 9). If this occurs in a bifurcation, devices can buckle into the wrong vessel. In this case, proximal advancement is not translated to the tip, and a large loop is formed (10, 11) (see Fig. 1C). Friction can also prevent the guidewire-catheter system from moving forward. Potential energy accumulates, stretching and stressing the vessels. In such conditions, it is difficult to anticipate the release of the accumulated energy, which may occur ballistically leading to vessel perforation (12). Friction and pushability problems can be mitigated by applying a hydrophilic coating on the outer surface of the device (13) and by optimizing the bending stiffness along the device (14). Increasing the stiffness comes with the drawback of making the devices too stiff to bend through certain anatomies, which can lead to substantial forces on the vasculature. Recent technical

advances in catheter and guidewire design have mostly been based on improving stiffness and friction properties to improve pushability.

Robotically assisted endovascular interventions promise to again revolutionize the operating room, improving clinical outcomes and reducing workplace-related hazards for the operator. These interventions are achieved through added sensing, software functionalities and automation algorithms and have the potential to reduce ionized radiation exposure for both patients and operators, as well as reduced procedural times and improved surgical outcomes (15–17). Additionally, being able to operate remotely in a telerobotic setting has great potential to make this life-saving intervention accessible to more people around the globe, particularly to those living in rural regions. Endovascular robots first made their way into the operating room in 2012 with the launch of the Magellan™ robotic platform (Johnson & Johnson Inc., Redwood City, CA, USA) for peripheral vascular interventions (PVI) (18, 19). These types of robotic systems have experienced a recent renaissance with the CorPath GRX® (Siemens Healthineers International AG, Waltham, MA, USA) and R-one™ (Robocath Inc., Rouen, France) systems (20). Despite the advantages offered by these robotic platforms, they primarily concentrate on steering traditional passive pre-shaped guidewires and catheters, employing motorized advancer units that mimic human actuation. Although this approach adds remote steering capability, it does not address the inherent limitations related to friction, buckling, and steerability found in traditional manual devices.

Substantial efforts have been dedicated to the development of actively steerable and deflectable devices to enhance device steerability. Different technical solutions for distal tip steering have been proposed with the common objective of increasing device maneuverability. The underlying technologies range from hydraulic (21–25), acoustic (26), and shape memory alloy (27–31) solutions, to tendon-driven (32, 33) continuum robots. Although these solutions offer active steerability, they require lengthy tubing and cabling to connect the actuators and pumps to the device tip, which can be susceptible to issues like hysteresis and nonlinear backlash (34). In contrast, magnetically steered continuum robots, another class of actively steerable devices (35), do not suffer from the shortcomings.

A magnetic continuum robot (mCR) is a device with embedded magnetic material that is steered through remote magnetic navigation (RMN) (36). In RMN, the mCR's distal tip is wirelessly steered by an external magnetic field that applies a magnetic torque on the embedded magnetic material. The magnetic fields – which are usually lower than 150 millitesla (mT) – are generated by a magnetic navigation system (MNS), a machine specifically designed to generate external magnetic fields for mCR steering (35). Generally, an MNS either uses large permanent magnets that are moved on a robotic arm (37) or stationary electromagnets, in which case the system is called an electromagnetic navigation system (eMNS) (38). RMN has been of increasing interest for minimally invasive surgeries including cardiac ablations (39) and neurovascular interventions (40, 41) because of its potential benefits in speed and accuracy (17). Both electromagnetic navigation systems and permanent-magnetic navigation systems have been commercialized (42, 43). In conventional catheterization, guidewire selection and shape are key factors for success (44) and are critical challenges facing clinicians when preparing for an intervention (45). Magnetic navigation offers the advantage of adaptive reshaping of the magnetic distal tip during the procedure.

We present a highly dexterous robotic device, designed to navigate the dense and tortuous arterial structure of the brain (46). We use a locomotion modality that overcomes pushability

and trackability limitations by coupling insertion with rotation and by adding a helical protrusion on the outer surface of the device. The protrusion engages with the vessel wall, analogous to a flexible screw, and pulls the device forward when rotated (see Fig. 1A). The rotation is induced at the proximal part of the device and transmitted towards the distal part along its torque-transmitting body. This actuation principle, combined with magnetic steering, enables the dexterity and navigability necessary to access hard to reach target locations in the vascular system. The segmented articulating magnetic tip design makes the device tip soft and atraumatic and yet maximizes the actuatable tip deflection angle (see Fig. 1B). The helical device's effectiveness is demonstrated through successful navigation experiments conducted in silicone models of the human vasculature, in an ex vivo human placenta, as well as in an in vivo porcine model.

## RESULTS

### Robotic system design

Our robotic platform consists of a helical mCR that is steered by external magnetic fields generated by an eMNS (Fig. 2C). The eMNS consists of three electromagnets in a triangular arrangement (see Fig. 2B and section "Electromagnetic navigation system"), positioned on the cranial side of the patient. The height of the electromagnet array can be moved to match the height of the patient bed. The mCR is advanced by a motorized advancer unit mounted on a surgical arm attached to the patient bed (Fig. 2D). The operator steers the mCR via a dedicated user console (47) either beside the patient or from a remote location in a teleoperation setting (Fig. 2A). Visual feedback is provided through X-ray images generated by a mono-planar fluoroscope imaging device (Fig. 2E). The subunits are interfaced with the Robot Operating System (ROS) (48) because of its high degree of modularity and simple multi-threading capabilities.

### Helical magnetic microcatheter and guidewire design

We have developed two implementations of the helical mCR design concepts that are tailored to navigate in the millimeter-sized cerebral arteries, such as the M1 (mean inner diameter (ID) of 3.1 mm) and the more distal M2 (mean ID of 2.4 mm) segments of the middle cerebral artery (MCA) (49). Both implementations comprise a torque transmitting backbone with a helical protrusion on its outer surface (outer diameter (OD) 0.7 mm with helix) and an articulating magnetic tip (OD 0.8 mm). The first implementation is a steerable helical guidewire (see Fig. 3A), the second a steerable helical microcatheter (see Fig. 3B).

The guidewire version has a tapered nitinol thread core for tip stiffness optimization. An optimized stiffness gradient is crucial for navigating extremely tortuous anatomies (45). In the case of the microcatheter version, the inner lumen was left empty to enable fluid injection. An in vivo fluid injection can be seen in video S3 of the Supplementary Materials. The devices are sufficiently small to be deployed using both a trans-radial (4-6 Fr) and a trans-femoral (5-9 Fr) approach through a conventional intermediate catheter. For an effective implementation of the rotating locomotion principle, torque transmission along the mCR is crucial. If the device is too torsionally elastic, the rotation applied to the proximal end may not be effectively transmitted to the distal tip. This can result in imprecise tip control, similar to backlash behavior, and in severe cases, sudden releases of the accumulated energy. To meet the torquability and flexibility requirements, a multi-filar

stainless steel torque coil was used as a torque transmitting backbone. The non-destructive bending radius of the device's most distal section is less than 5 mm.

### Advancer unit design

Advancing helical devices requires not only linear translation but also rotation, in contrast to traditional mCRs (41, 50). To address this requirement, we developed a remotely controlled, motorized advancer unit that pushes and rotates helical mCRs (see Fig. 3C). It can accommodate devices of different diameters and pitch angles, and has unlimited driving length due to a friction-roller-drive-mechanism (20). The helical mCR is clamped against the motorized roller by a grooved guiding insert at an angle such that the mCR is simultaneously translated and rotated (see Fig. 2D). The pitch angle can be adjusted by replacing the plate which holds the guiding insert (see fig. S1 in the supplementary materials). To retract the helical device, the friction roller of the advancer is actuated in the inverse direction, causing a backwards translational and rotational motion of the device. For more adaptability during surgery, the advancer was mounted on an adjustable surgical arm that is attached to the surgical bed. The passive components are autoclavable and a sterile barrier in the form of a plastic drape is used to protect the motor.

### Reachable workspace

To determine the behavior of the mCR tip in open spaces, we investigated its reachable workspace experimentally by performing a parameter sweep of the insertion length and magnetic field orientation (see Fig. 4A and B). The reachable workspace of an mCR is tightly coupled to the feasible workspace of the eMNS (for definition see (51)).

To define the workspace for a given robotic task, the mCR and eMNS were considered as one system. Boehler *et al.* have provided a systematic methodology and a toolbox to determine the workspace of eMNSs (51). The magnetic-feasible workspace of the three-coil eMNS at z-height 0 mm is illustrated in Fig. 4B given the desired set of magnetic tasks  $\mathcal{D}$ :

$$\mathcal{D} = \{\mathbf{b} \in \mathbb{R}^3 \mid 5 \cdot 10^{-3} \text{ T} \geq \|\mathbf{b}\|_2\} \quad (1)$$

where  $\mathbf{b} \in \mathbb{R}^3$  is the magnetic field generated by the eMNS.

The large magnetic volume and the flexible articulating links of the mCR tip enable tip deflections over  $90^\circ$  and steerability even at small fields of 5 mT (see Fig. 4A). This allows for active tip steering from the aortic arch to the cerebral arteries. The reachable tip workspace with an overlay of the vascular anatomy is shown in Fig. 4B. Fig. 4A shows that increasing the external magnetic field strength above 35 mT does not substantially affect tip reachability.

### Helix effectiveness

To validate the effectiveness of the helical protrusion at transforming rotation into translation, the mCR was tested in a flat vessel model with multiple consecutive turns and with interchangeable lumen materials (see Fig. 4C). The devices described in this section

were actuated manually by hand by either combining translation and rotation in both clockwise or counter-clockwise direction, or by pure translation.

First, the performance of the helical mCR was evaluated by comparing it to the same device with no helix. The helix-free device is actuated by both rotation and translation, and pure translation, whereas the helical device is actuated by clockwise rotation and translation (Fig. 4D). The devices were inserted in a silicone lumen of shore hardness 60A. Silicone is commonly used in the fabrication of vascular models and has similar mechanical properties to cranial blood vessels (52). Fig. 4D shows that the helical mCR could advance 14 turns before friction became too high to further advance the device, compared to the mCR with no helix, which advanced 4 turns.

Furthermore, the results in Fig. 4D indicate that rotation, in itself, improves advancement. The helix-free device which is rotated and translated, advanced further than the one that was purely translated (4 turns compared to 2 turns). This can be explained by the fact that a rotating device can be maintained in a dynamic friction regime, even when it is not advancing. In contrast, a purely translated device must overcome static friction every time it is not advancing.

To further evaluate the effectiveness of the helix, the mCR was inserted into the model with clockwise rotation and translation, counter-clockwise rotation and translation, and pure translation (see Fig. 4E). When rotated counterclockwise, the helix counteracted the forward advancement. The results shown in Fig. 4E indicate the effectiveness of the helix, as the clockwise actuated mCR advanced 7 times further than the mCR that was actuated in a counter-clockwise direction or translated without rotation.

To demonstrate that the helix engages with the soft lumen wall, the helical mCR was inserted in lumens made from materials with increasing hardness (polytetrafluorethylene (PTFE) and polymethyl methacrylate (PMMA)). Hard surfaces reduce the engagement of the helix and, thus, its forward pushing effect. Fig. 4E shows that the forward rotated helical mCR managed fewer turns with increasing lumen hardness. In contrast, the inversely rotated and pushed mCRs advanced by almost the same amount, regardless of the lumen hardness.

### **In vitro navigation in human vascular model**

Accessing the target site in the brain using the conventional manual technique involves multiple steps. The process begins by inserting a guiding catheter through either the leg (trans-femoral approach) or the arm (trans-radial approach) and advancing it beyond the aortic arch into the neck arteries. The guiding catheter is then used as an anchor point to deploy and stabilize additional catheters and guidewires. Typically, the guidewires lead the way and act as a rail over which the flexible intermediate catheters are deployed. Depending on the depth and size of the target vessel, additional sets of microwires and microcatheters are inserted. Mastering this procedure requires a high level of skill and may involve multiple attempts, often requiring the exchange of devices. Inserting multiple devices prolongs procedure time, and increases the risk of arterial endothelial injury. Reducing the number of catheters and guidewires increases clinical efficacy and procedure speed while reducing fluoroscopy time and mitigating the risk of adverse events (16, 17).

Here, we demonstrated that our helical mCR can be used as an all-in-one device and is capable of navigating through complex anatomies. The device was navigated in a silicone model of human vasculature. Four navigation tasks were investigated that are challenging to perform with conventional manual devices. The first task consisted of navigating to distal millimeter-sized anterior cerebral vessels (MCA-M2 segments) through the trans-radial access path. Although the trans-femoral approach is commonly preferred due to the relatively straight path from the leg to the neck, the trans-radial approach has gained recognition as a feasible alternative due to the lower rate of local vascular complications. However, the trans-radial approach is less commonly used due to the more challenging anatomical features (2). The magnetic field strength in the region of the aortic arch ranges from 5-15 mT and in the cerebral arteries from 20-30 mT (see Fig. 4B).

Fig. 5A depicts the navigation of the sharp turn between the subclavian artery (SA) and common carotid artery (CCA). As can be seen in video S2 of the Supplementary Materials, the mCR did not buckle at the SA-CCA bifurcation and showed high steerability in the tortuous cerebral arteries.

In the second task, the helical guidewire was used as a delivery tool to guide with 1.17 mm ID and 1.67 OD (5 Fr) intermediate catheter to the cerebral arteries. In the treatment of stroke, intermediate catheters are commonly used for decannulation to aspirate blood clots or to deliver mechanical thrombectomy devices. The deployment of the catheter is depicted in video S2 of the Supplementary Materials.

In task three (Fig. 5B, and video S2 of the Supplementary Materials), the helical mCR was navigated across a morphological type III aortic arch through the trans-femoral approach without buckling. Type III aortic arches are particularly difficult anatomic variations of the aortic arch and are related to a higher complication rate in cranial reperfusion (7). The variation occurs in 20 % of the stroke patients eligible for mechanical thrombectomy (53).

The fourth task consisted of crossing a fusiform giant aneurysm by navigating the helical mCR from the internal carotid artery (ICA) to the distal parent artery of the fusiform giant aneurysm (Fig. 5C). Fusiform giant aneurysms have a dome diameter of over 25 mm and are particularly challenging to treat for manually steered guidewires. These guidewires often lack the necessary shape and sufficient lateral support, leading to buckling, which may necessitate multiple attempts, reshaping of the tip, and/or the use of additional catheters (54). In contrast, the magnetic tip of our device provides three-dimensional tip control that facilitates targeting the parent arteries, and the helix can push itself forward inside the aneurysm preventing loop formations, as shown in video S2 of the Supplementary Materials.

During navigation, we observed some slight vibration of the tip. We can attribute this behavior to the device's overall geometry. The 1700 mm long device may not always be perfectly straight, especially if it is not stored in a straight tube. This slight curvature could result in a small rotational imbalance. However, we have yet to encounter navigation issues caused by this imbalance, and we believe that more controlled manufacturing and storage methods could eliminate the effect.

#### **Invasiveness study in ex vivo human placenta model**

To evaluate the potential mechanical impact on the vessel wall, we conducted an invasiveness study using a helical mCR in an ex vivo human placenta (see Fig. 6A).



Placentas are particularly suited for endovascular device testing because they are similar in size and curvature to human intracranial arteries (55, 56). We chose the placenta veins because they carry oxygenated blood, similar to the cerebral arteries (56), and are simpler to access and characterize (55). In this experiment, we collected a placenta immediately after birth to enable testing in blood vessels that have intact endothelial cells, which enabled the assessment of the condition of the individual vessel wall layers at the histological level.

The helical magnetic guidewire was inserted and retracted 20 times at an insertion speed of 5 mm/s and a corresponding rotation speed of 5 turns per second in one of the placenta veins (see Fig. 6B). For comparison, a non-magnetic commercial guidewire (.035 Glidewire, Terumo Medical Corporation, New Jersey, USA) was also inserted and retracted 20 times in a separate blood vessel. To establish upper and lower reference points for physical impact assessment, both positive and negative controls were implemented (see Fig. 6B and C). The positive control was established by intentionally inducing damage to the cell layers using a sharp metal wire tool (see Fig. 6C, “Positive control”). The negative control refers to the blood vessel into which no device had been inserted, leaving it unharmed. Following the experiments, the tested placenta immediately underwent fixation by 4% formalin for 48 hours, followed by a histological analysis specifically at the levels of the areas of insertion of the different devices to assess of the condition of the vessel wall layers. The analysis was performed by an expert pathologist who received the samples in a blind test.

The histological analysis of the negative control displayed an intact endothelial cell layer and vessel wall (see Fig. 6D “Negative control”), whereas the positive control demonstrated notable disruption of the inner vessel wall, including complete separation and missing portions of the endothelium (see Fig. 6D “Positive control”). These controls effectively established a lower and upper reference for evaluating the extent of damage.

The analysis revealed that the helical guidewire had a minor physical impact on the vessel wall, as indicated by minimal separation of areas of the endothelium from the subendothelial stroma (see Fig. 6D “Helical guidewire”). These cell layer detachments can be attributed to friction between the device and the vessel wall, resulting in shear forces that led to the detachment of the cell layers. Similarly, the commercial guidewire displayed minor but slightly more damage in several locations in the form of endothelial detachment and small stromal tears, indicating slightly higher shear forces (see Fig. 6D “Commercial guidewire”).

### **In vivo navigation in a porcine model**

To demonstrate the validity and efficacy of the technology in a clinical setting, an in vivo feasibility study in a porcine model was performed. Porcine vessels are commonly utilized in research as models for human vessels due to their comparable size, anatomy, and general function (57). They enable the simulation of complete cranial interventions, starting from the placement of larger guiding catheters through transfemoral access across the aortic arch to the navigation within small-sized arteries. Such experiments are a first and important step towards applications in humans.

The first navigation showcases the device's ability to achieve distal access by navigating through narrow and tortuous arteries. The device was inserted through the femoral artery via a commercial 5 Fr vertebral catheter (Impress® Diagnostic Peripheral Catheters, Merit Medical Systems Inc., Utah, USA) into the external carotid artery (ECA) and navigated to the millimeter-sized ethmoidal artery (EA) (see Fig. 7). To highlight the effectiveness of the

working channel, a fluid injection was performed. One prominent application scenario is angiography, in which a liquid contrast medium is injected to enhance the visualization of blood vessels during X-ray imaging. This technique allows otherwise invisible blood vessels to be clearly seen. In addition, fluid injection through the working channel can also be utilized for therapeutic interventions. For example, the administration of anticoagulants can support the dissolution of blood clots during stroke treatment, whereas embolization agents are injected to deliberately block blood vessels in the management of arteriovenous malformations. After performing angiography in the EA, the device was fully retracted and navigated to the facial artery (FA) where so-called super-selective angiography was performed. Super-selective angiography is the local injection of contrast agent to reveal small blood vessels.

After retraction back into the ECA, the magnetic device was navigated into the caudal auricular artery (CAA) to demonstrate the device's high steerability in low magnetic fields. Notably, the CAA presented a challenging scenario with a sharp bifurcation angle exceeding  $90^\circ$ . At the bifurcation between the CCA, the maxillary artery (MA) and the CAA, the magnetic catheter tip was 320 mm away from the magnetic coils of the eMNS. At the given distance, the magnetic field was 10 mT. Three attempts were needed to enter the CAA. The main challenge lay in the CAA orientation that was pointing out-of-plane. Note that what appears to be the catheter exiting the blood vessel in Fig. 7, fig. S2, and the corresponding video S3 in the Supplementary Materials is, in reality, a shift between the roadmap and the vessels observed in real-time.

Postinterventional analysis demonstrated that in the first two attempts, the device was oversteered with an offset angle (angle between the external magnetic field and the magnetic tip) of  $108^\circ$  and  $164^\circ$ , whereas in the successful attempt, the offset angle was  $74^\circ$  (see fig. S2 in the Supplementary Materials). One advantage of robotically assisted interventions is the ability to record and analyze such events.

### **Simulated navigation of the helical magnetic continuum robot**

Robotically assisted interventions facilitate data recording for post-interventional analysis, as demonstrated in the previous section and illustrated in fig. S2 of the Supplementary Materials. These interventions also provide the means to analyze, plan, and practice interventions on digital test benches. This requires high-performance simulators with a minimal gap between simulation and reality. To demonstrate the feasibility of realistic simulations, we developed a model of our helical mCR using the simulation framework described in (58), and enhanced it with a simple analytical model outlined in the "Analytical formulation of helix pushing force" section. Details of the simulator can be found in the "Simulation of the helical magnetic continuum robot" section.

We validated the simulator by comparing digital navigations (in silico) with the real in vivo navigation presented in the "In vivo navigation in a porcine model" section, as well as an in vitro navigation performed on a 3D printed model. The navigations exhibited high similarities in terms of dynamics and qualitative behavior. For a side-by-side comparison between the real and simulated navigations, please refer to Fig. 8 and video S4 in the Supplementary Materials.

## DISCUSSION

The locomotion paradigm we introduce is based on a helical protrusion on the device's outer surface that engages with the vessel wall (much like a flexible screw) and transforms a proximal rotation into a linear translation of its distal tip. When the helical mCR is at rest or stuck, rotation facilitates the transition from a static to a dynamic friction regime. For example, when the device starts to buckle, pushing will cause the device to collapse further and form a loop (see Fig. 1C). Thus, axial forces can no longer be transmitted preventing distal tip advancement and risking vessel perforation or dissection. Rotation, on the other hand, can still be transmitted along the axis of the device without increasing the axial load. Another favorable effect that comes from rotation is the incremental release of elastic energy. Rotation promotes the propagation of small elastic deformations from back to front in a wave-like manner, instead of releasing large deformations ballistically. Furthermore, the helical protrusion on the outer surface gently engages with the vessel wall and translates rotation to axial advancement. At every point of contact the rotating helical continuum robot slightly pulls itself forward. This also facilitates the passage of bifurcations, where a conventional device is more likely to buckle (see Fig. 1C and video S2 from the Supplementary Materials).

In manual catheterization, the devices are primarily actuated by pushing, but rotation is used as well, mainly to redirect the pre-shaped device tip and occasionally to facilitate thrombus penetration (59). Rotation is tightly coupled with tip steering and, therefore, its use for locomotion purposes is limited. Endovascular robots such as the CorPath GRX<sup>®</sup> system (Corindus Inc., Massachusetts, USA) use motorized advancers to translate and rotate pre-curved endovascular devices, replacing the operator's hand motion by motorized actuators. The CorPath GRX<sup>®</sup> has the same disadvantages as manual operation, where rotation is mainly dedicated to steering and cannot be independently utilized for locomotion. Although the CorPath GRX<sup>®</sup> advancer is technically compatible with our devices, it lacks the necessary magnetic actuation required to utilize the rotational locomotion principle. A magnetically steered tip maintains a chosen tip direction even when the device is rotated around its longitudinal axis.

Non-magnetic screw tip continuum devices have been proposed but are either designed for large-scale gastroscopic applications (60), or to drill through thrombi in the vasculature (61, 62). Our device uses a helical protrusion along its entire length to translate contact points with the vessel wall into forward propulsion. Untethered helical magnetic devices have been proposed for vascular navigation (63–70) and for thrombi penetration (71–75). The devices promise a versatile range of applications due to their wireless nature. However, the functionalization of the devices is limited by their small size and the technology has yet to prove itself in a clinical environment.

Tethered magnetic screw-tip devices have also been proposed. Yu *et al.* (76) and Sperry *et al.* (77) demonstrate navigation of a magnetically actuated spiral guidewire for blood clot penetration and a magnetically steered flexible screw-tip needle for soft tissue navigation in the brain. In both approaches, the spiral structure is concentrated at a short and rigid screw-like tip. Although the rigid tip design and localized tissue engagement at the tip may be adequate for soft tissue drilling, the pulling forces are likely to be inadequate for locomotion in the vasculature. To generate effective pushing forces, the helix must have direct contact with the surrounding soft tissue. In applications such as liver or brain penetration, constant tissue contact allows the screw tip to generate enough pulling force to propel the rest of the device. However, in endovascular navigation, open spaces in blood vessels can cause loss

of contact with the vessel wall. Spreading the helix along the device body establishes multiple contact points, ensuring continuous tissue contact and tip-independent pushing forces. Furthermore, by extending the helix along the body of the device, the local pushing forces are reduced, which in turn reduces the risk of tissue trauma, which our histology tests confirm. In the section “Invasiveness study in ex vivo human placenta model”, we measured potential tissue trauma. The results of the invasiveness study indicate that our helical magnetic device causes minimal damage to the vessel wall, with less detectable damage compared to a commercial guidewire.

Although these findings are promising, they represent only the initial safety tests in a series of comprehensive evaluations required for regulatory approval before the device can be used in humans. Given the distinctive characteristics of the helical device, obtaining FDA registration will require clinical data from extensive in vivo studies involving multiple animals, including post-mortem assessments, followed by subsequent human studies. In addition to these studies, comprehensive risk management will involve further investigation to demonstrate the safety and efficacy of the technology, including design, materials, manufacturing, and usability. Evidence of the system's safe and intuitive operation will be required, as well as quantifying and comparing procedure times to those of legally marketed devices. The execution of in vivo trials and usability studies will require rigorous statistical analysis and a number of participants.

For conventional manual interventions, radiologists use their hands to manipulate guidewires and catheters, allowing them to perceive small variations in friction during the insertion process. Our system lacks this type of tactile and haptic feedback due to the absence of force sensing at the level of the advancer unit. Although advancer units with force sensing have been proposed (78), the reliable implementation of force data that radiologists can rely on remains a challenge since the forces generated at the device tip are small and are partially dissipated along the path to the sensor by device deformation, friction between insertion sheaths, hemostasis valves, advancer gears, and friction rollers. This is likely why commercial non-magnetic robotic systems, such as the CorPath GTX<sup>®</sup>, have not integrated force sensing functionality. Furthermore, studies utilizing commercial systems do not report any challenges or adverse events related to the absence of haptic feedback (79, 80). This can be attributed to the fact that radiologists primarily rely on the rich visual information provided by X-ray imaging, allowing them to detect subtle changes in device behavior and deformations. However, the ability to recognize hazardous situations based on X-ray images requires years of experience. To provide assistance to the operator, sensor-less software algorithms based on X-ray images for the measurement of contact forces have been proposed, which could potentially eliminate the need for additional sensors (81).

The main focus in commercial magnetic actuation systems such as Stereotaxis Genesis RNS<sup>®</sup> has been in increasing the magnetic field strength (0.08-0.12 T) (42) to achieve better device steerability. This compensates for the limited magnetization of the magnetic devices but requires powerful machines that have a large footprint and require permanent installations. As mobile and small footprint eMNSs with low magnetic fields in the 20-30 mT range move towards clinical application, the importance of magnetic device design becomes more relevant. Rather than increasing the external magnetic field magnitude, steerability can be improved by increasing the magnetic moment of the steerable device tip and decreasing its bending stiffness. Traditionally, mCRs are designed with one or more strong but rigid distal permanent magnets, connected by flexible tubular sections (35, 36, 50, 82–84). This approach has an inherent trade-off: for a fixed length, more magnetic

volume necessarily requires longer rigid magnetic sections and, therefore, less overall flexibility. Alternatively, steerable mCR tips can be made from soft polymeric materials doped with magnetized particles (85, 86). Kim *et al.* demonstrated the effectiveness of this approach for neurovascular applications. Although these mCRs can be made soft and flexible, the magnetic moment of the magnetized polymers is considerably lower than rigid permanent magnets, requiring larger external magnetic fields (30 -80 mT) (41). In contrast, our magnetic device, which incorporates articulating permanent magnets, operates effectively at low magnetic fields below 30 mT and offers steerability even at fields as low as 5 mT (see Fig. 4A).

Related magnetic tip designs using spherical magnetic chains for magnetic actuation was modeled and analyzed by O'Donoghue *et al.* (87), and Hong *et al.* (88) shows the application of a single ball joint magnetic tip, designed for flexible needle steering in deep brain stimulation. Furthermore, Pittiglio *et al.* (89) presented workspace characterizations and closed-form kinematic modelling of a highly steerable ball chain robot. Here, we introduce a submillimeter device that incorporates a usable working channel. The design consists of interconnected hollow cylinders with rounded surfaces that function as articulations. The working channel of the device serves multiple purposes, including fluid injection and the delivery of various endovascular devices. Furthermore, it can be utilized to create a stiffness gradient along the magnetic tip, enabling improved navigation through highly tortuous blood vessels. Combining this with our helical actuation principle enhances the maneuverability and effectiveness of the device for navigation in complex vasculature.

The MNS used in this work is an eMNS with a small footprint. Due to their compact size, light weight, and mobility, these systems offer higher acceptance and easier integration into hospital workflows. Light-weight permanent magnet MNS also exist, such as (37, 41, 90). Kim *et al.* (41) proposed a platform for neurovascular applications that utilized a single cylindrical NdFeB magnet, mounted on a 7-degree-of-freedom KUKA robot arm. However, unlike permanent magnet systems, eMNSs have the advantage of having no moving parts. This eliminates the need for complex robot arm motion planning to avoid collisions with equipment and personnel in the operating room and/or obstruction of the X-ray view. Additionally, the ability to deactivate the electromagnets can be a critical safety feature during interventions and when the system is not in use.

Despite the advantages of eMNSs, the helical mCR presented in this article is compatible with any MNS and therefore, could be used in combination with the system described in (41). In their setup, the permanent magnet needs to be positioned close to the patient and must move with the mCR to generate sufficiently high magnetic torques and forces at the tip of the device. However, this restricts the maneuverability of the robot arm and makes motion planning more complex. The low-field steering capability of our device would increase the workspace of the permanent magnet, thereby expanding its range of motion. Furthermore, (41) reported a tendency for device buckling when navigating through artificial blood clots. The helical locomotion principle employed by our device could potentially enhance mCR navigation in such challenging situations.

Simulators, such as the one we presented (see Fig. 8 and video S4 in the Supplementary Materials), are an ideal platform for the training of neural networks, as they can produce large amounts of simulated training data at a relatively low cost (91, 92). Simulators also have the ability to extract otherwise inaccessible data, such as contact forces. Alternatively, robotic systems like ours can be used to record intraoperative data (see section “In vivo

navigation in a porcine model” and fig. S2) to build large databases for analysis and the development of machine learning algorithms. Machine learning based motion planning algorithms have been proposed for autonomous device navigation (91, 93, 94). However, to translate these simulation-based algorithms to the real world, it is essential to minimize the gap between simulation and reality. Although the in vivo and simulated navigations presented in Fig. 8 and video S4 in the Supplementary Materials exhibit high similarity, a limitation of our simulation framework lies in the lack of fine details, such as small side branches, in which the device could get caught, or the lack of blood flow modelling. Capturing these details in the simulation will be essential to reduce scenarios in which the system does not behave as required. These unforeseen scenarios are often referred to as “edge cases”. In some artificial intelligence (AI) applications, edge cases might be acceptable. However, when it comes to automating navigation tasks in medical applications, small problems can often have large consequences. Medical robots interact with the physical world and therefore, there is the potential for real damage to be inflicted.

In the case of commercial neurovascular robots, decision-making and motion control are still exclusively in the realm of the surgeon (autonomy level 0 in the classification proposed by Yang et al. (95)). However, these robotic platforms offer FDA-approved software features, such as automated guidewire rotation, to assist the crossing of thrombi (20). Progressing to higher autonomy levels will require more time, primarily due to numerous unsolved regulatory and liability questions (96). Another challenge with advancing autonomy in neurovascular robotics into clinical practice is the restricted access to live X-ray images that could be used for online image processing. Many fluoroscope device manufacturers withhold permission for third-party processing of their X-ray images, for safety and proprietary related reasons. Nonetheless, research laboratories have demonstrated the exciting perspectives and benefits of autonomous device navigation (96). Early adoption of autonomous features may be applicable in high-risk, high-reward applications where alternative options are limited. One particularly promising application is the teleoperated treatment of stroke, where increased autonomy could potentially provide patients in rural areas with better access to this life-saving treatment (97).

## MATERIALS AND METHODS

### Remote magnetic navigation

The eMNS was modeled with the linear mapping

$$\mathbf{b}(\mathbf{p}) = \mathbf{A}(\mathbf{p})\mathbf{i}, \quad (2)$$

which enabled computation of the electromagnetic currents  $\mathbf{i} \in \mathbb{R}^n$  needed to generate a desired magnetic field  $\mathbf{b}(\mathbf{p}) \in \mathbb{R}^3$  at any position  $\mathbf{p}$  in the eMNS’s workspace. The actuation matrix  $\mathbf{A} \in \mathbb{R}^{3 \times n}$  is system-dependent and was calibrated experimentally using the method described in (98), where  $n$  is the number of electromagnets. In the case of the eMNS used in this work,  $n$  was 3. The external magnetic field induced a magnetic torque  $\mathbf{t}_{mag} \in \mathbb{R}^3$  on the mCR’s magnets:

$$\mathbf{t}_{mag} = \mathbf{m} \times \mathbf{b}(\mathbf{p}). \quad (3)$$

This equation shows that the magnetic torque scales with the misalignment between the magnetic field direction  $\mathbf{b}(\mathbf{p})$  and the magnetic dipole moment  $\mathbf{m}$ . The magnetic forces induced by the magnetic field gradient had a minimal effect on the mCR tip and were therefore neglected.

### Electromagnetic navigation system

The eMNS used in this work is the Navion system, a preclinical device developed by the Multi-Scale Robotics Lab (MSRL, ETH Zurich, Zurich, Switzerland) and commercialized by Nanoflex Robotics AG (Nanoflex Robotics AG, Zurich, Switzerland). It is based on three electromagnets arranged in a triangular pattern. The electromagnets are mounted on a triangular yoke with a side length of 550 mm. The eMNS can generate a continuous current of up to +/- 35A for each electromagnet and has a workspace of 200 x 200 x 400 mm in which a magnetic field of 5 mT can be directed in any direction. The magnetic field strength at a distance of 200 mm from the surface of the electromagnets is 25 mT. The eMNS has a footprint of 1200 x 720 mm, and has been designed with wheels for easy mobility. Additionally, the height of the electromagnets can be adjusted to match the height of the patient bed.

### Torqueable backbone

The torque transmitting backbone consists of a custom double-layered, multi-filar torque coil (Asahi Intecc Co. Ltd., Aichi, Japan). Each layer comprises eight 0.06 mm 316 stainless steel filars, wound tightly adjacent to one another. Adjacent layers are wound in opposite directions. The construction is similar to a hollow flexible shaft. The helix has a pitch length of 1 mm and is tightly wound on the outer surface of the torque coil and laser welded at the ends. To reduce its stiffness and diameter, the most distal 100 mm was left partially uncovered (sleeve body design (44)). To reduce the risk of kinking and buckling, and to improve pushability, the device was reinforced proximally with 50  $\mu\text{m}$  thermoelastic Pebax<sup>®</sup> jackets to achieve the desired stiffness gradient along the central axis of the device. The distalmost jacket is 10 mm long with a shore hardness of 40D, followed by another 10 mm, 63D jacket, and a 72D jacket covers the remaining proximal section. The jacket was fused on the backbone coil using reflow lamination techniques. At the intersection of the Pebax<sup>®</sup> layers, the polymers melt together, producing a seamless transition between the sections. To further reinforce the most proximal part, a 38  $\mu\text{m}$  polyester layer was added on top of the 72D Pebax<sup>®</sup> layer up to 30mm from the 60D/72D intersection.

### Magnetic tip

There are two magnetic tip versions (see Fig. 3): one for the helical microcatheter and one for the magnetic guidewire. Both articulating magnetic tips comprise multiple hollow cylindrical magnets with adjacent convex surfaces. The segments have an OD of 0.7 mm and an ID of 0.17 mm, are made from gold coated neodymium-iron-boron (NdFeB), and are encapsulated in a 50  $\mu\text{m}$  35D Pebax<sup>®</sup> jacket.

In the microcatheter version, the inner lumen was left empty (see Fig. 3B) whereas in the guidewire version the lumen was used to add a stiffness gradient along the magnetic tip (see Fig. 3A). A smooth gradient between the device tip and the body can be important when

navigating sharp turns. If the transition between different stiffnesses is too abrupt, the magnetic tip can kink, making it impossible to further insert the device. The stiffness gradient was achieved by incorporating three 0.05 mm nitinol wires with different lengths, resulting in a tapered core shape with an OD of 0.1 mm at its thickest and 0.05 mm at its thinnest end.

### **Advancer unit**

The advancer consists of three parts: the main block, holding all the moving parts such as the friction drive wheel, gears, shafts, and the like, the clamping plate, containing the grooved guiding insert, and the motor and surgical arm mount. The mCR is clamped between the friction roller and the guiding insert. Clamping can be adjusted by tightening a large thumb screw, which adjusts the distance between the main block and the clamping plate. The friction roller is made from silicone rubber and the guiding insert from transparent polycarbonate (PC). The guiding insert has a groove that keeps the device centered and in contact with the drive. The guiding insert is held at an angle to the drive wheel corresponding to the pitch angle. A transparent material for the guiding insert was chosen so that the alignment of the mCR and the contact with the roller can be visually inspected and verified. The angle between the guiding insert and the drive wheel was adjusted by replacing the entire clamping plate with a clamping plate containing a guiding groove with different pitch angle. Hence, the pitch angle can be adjusted when the mCR is exchanged but not during operation. The main block can be detached from the motor, allowing the motor to be covered with a sterile drape, while the main block and clamping plate can be removed and autoclaved for sterilization. The device inlet and outlet are compatible with Luer-Locks, which allows the attachment of connectors and guiding tubes. The advancer unit was attached to a surgical arm (FISSO, Zurich, Switzerland) and directly mounted on the patient bed. A Maxon DCX 12 motor (Maxon Group, Sachseln, Switzerland) was used to drive the roller, controlled with an EPOS 4 (Maxon Group, Sachseln, Switzerland) position controller, and powered by a 12 V power supply. Gear reduction from the driving motor shaft to the roller shaft was 159:1. With a roller diameter of 25.4 mm and an mCR diameter of 0.8 mm, the total motor to mCR reduction is 1:5.

### **Reachable workspace measurement**

The workspace measurement shown in Fig. 4A was performed in an eight-coiled eMNS called the CardioMag eMNS (51). The CardioMag can generate arbitrary three-dimensional homogenous magnetic fields in a workspace of 100 x 100 x 100 mm. The mCR was inserted through a fixed insertion point at discrete steps of 5, 10, 15, 20, 30 and 50 mm, and the magnetic field was rotated at every insertion length from 0° to the singularity point – the point at which the mCR flips to a more stable equilibrium position. At insertion lengths above 20 mm, a small upwards-pointing field component was applied for gravity compensation. The mCR distal tip was tracked with an optical color marker tracker. To this end, green and red markers were painted on the mCR tip and filmed with a Basler acA1920-48gc GigE camera (Basler AG, Ahrensburg, Germany). The image processing pipeline used for tip detection consists of an HSV threshold for green and red color, followed by a maximal distance limit threshold to discard false detections. The tracked tip path was filtered in post processing using a first order Butterworth filter with a cut-off frequency of 0.024, normalized to the Nyquist frequency.

### **Setup of the helix effectiveness experiment**



The experimental setup shown in Fig. 4C is made from three PMMA plates that have been screwed together. The middle plate has cutouts that hold and guide a plastic lumen made from materials with different hardness that are filled with a water-soap solution, reducing vessel wall friction (17, 99). The first lumen is a silicone tube with shore hardness 60A, the second is made from PTFE with an intermediate shore hardness of 60D, and the last and hardest lumen, is made from PMMA with a shore hardness of 90D and a square lumen cross-section for easier manufacturing. Both the circular and square lumens have a diameter and a lateral length of 2 mm. The setups were backlit through a light panel and filmed with a Canon EOS 6D (Canon Inc., Tokyo, Japan) camera. The commercial guidewire used as reference is .035" Glidewire with hydrophilic coating (Glidewire, Terumo Medical Corporation, New Jersey, USA).

### **In vitro models of the human vasculature**

The helical guidewire was navigated in a silicone model (Trandomed 3D Inc., Zhejiang, China) containing the aorta, cerebral arteries and major arteries of the lower and upper limbs. Furthermore, a silicon model was fabricated containing the ICS, a fusiform giant aneurysm with dome diameter of 25 mm and the distal parent arteries. The commercial catheter used in the experiment is a 5 Fr intermediate / aspiration catheter (AXS Catalyst 5 aspiration catheter, Stryker Corporation, Michigan, USA). Given that the friction between real blood vessels and endovascular devices is generally very low (friction coefficient < 0.017 (99)), the addition of soap to the water has proven effective in reducing the friction between the devices and the artificial vessel wall made from silicone rubber, thereby bringing the friction closer to reality. This practice is widely adopted (17, 100) and is also recommended by the manufacturer of the vascular model.

### **In vivo experiment**

A 45 kg female domestic pig (*Sus scrofa domestica*, breed: Swiss large white; approximately 4 months of age) was placed under general anesthesia with continuous vital parameters monitored by a veterinarian team throughout the procedure. At the end of the procedure the pig was euthanized. The animal study was approved by the local Committee for Animal Experimental Research (Cantonal Veterinary Office Zurich, Switzerland) under license number ZH213/2019. The right femoral artery was catheterized with an introducer sheath (Avanti<sup>®</sup> + Introducer, 6F; Cordis<sup>®</sup>, Miami Lakes FL, USA) placed percutaneously under ultrasound guidance using the Seldinger method. To reach the ECA, a guiding catheter commercial 5 Fr vertebral catheter (Impress<sup>®</sup> Diagnostic Peripheral Catheters, Merit Medical Systems Inc., Utah, USA) was placed in the introducer sheath through which the mCR was inserted. A prophylactic dose of heparinized saline was applied (activated clotting time (ACT): 104 seconds). Imaging was performed with a mono-plane angiography system (Allura Xper FD20 fluoroscope, Philips N.V., Amsterdam, Netherlands). The horizontal distance between the fluoroscope center and the surface of the eMNS is 340 mm. At the given distance, the magnetic field in the fluoroscope's field of view ranges from 5 mT at the lower edge to 25 mT at the upper edge of the image. The helical magnetic microcatheter described in "Helical magnetic microcatheter and guidewire design" was used and advanced with the advancer unit presented in "Advancer unit design". The intervention was performed by an experienced interventional neuroradiologist. Navigation was done at the bedside. All system inputs and outputs are recorded for analysis. The mCR navigation was performed under fluoroscopic control using roadmaps in different extracranial pig vessels. Angio runs

were performed using contrast agent (Ultravist, Iopromid, Bayer Vital GmbH, Germany) saline solution.

## **Supplementary Materials**

Methods

Figs. S1 to S3

Table S1

Movies S1 to S4

## References and Notes

1. V. Saini, L. Guada, D. R. Yavagal, Global Epidemiology of Stroke and Access to Acute Ischemic Stroke Interventions. NLM (Medline) [Preprint] (2021). <https://doi.org/10.1212/WNL.0000000000012781>.
2. Z. Wang, J. Xia, W. Wang, G. Xu, J. Gu, Y. Wang, T. Li, Transradial versus transfemoral approach for cerebral angiography: A prospective comparison. *Journal of Interventional Medicine* **2**, 31–34 (2019).
3. S. A. Munich, K. Vakharia, E. I. Levy, Overview of Mechanical Thrombectomy Techniques. *Clin Neurosurg* **85**, S60–S67 (2019).
4. P. Candio, M. Violato, J. Leal, R. Luengo-Fernandez, Cost-effectiveness of mechanical thrombectomy for treatment of nonminor ischemic stroke across Europe. *Stroke*, 664–673 (2021).
5. H. B. van der Worp, J. van Gijn, Acute Ischemic Stroke. *New England Journal of Medicine* **357**, 572–579 (2007).
6. T. Brott, J. Bogousslavsky, Treatment of Acute Ischemic Stroke. *New England Journal of Medicine* **343**, 710–722 (2000).
7. F. J. A. Mont`Alverne, F. O. Lima, F. de A. Rocha, D. de A. Bandeira, A. F. de Lucena, H. C. Silva, J. S. Lee, R. G. Nogueira, Unfavorable vascular anatomy during endovascular treatment of stroke: Challenges and bailout strategies. Korean Stroke Society [Preprint] (2020). <https://doi.org/10.5853/jos.2020.00227>.
8. J. Kaesmacher, J. Gralla, P. J. Mosimann, F. Zibold, M. R. Heldner, E. Piechowiak, T. Dobrocky, M. Arnold, U. Fischer, P. Mordasini, Reasons for reperfusion failures in stent-retriever-based thrombectomy: Registry analysis and proposal of a classification system. *American Journal of Neuroradiology* **39**, 1848–1853 (2018).
9. S. Katz, S. Givli, The post-buckling behavior of a beam constrained by springy walls. *J Mech Phys Solids* **78**, 443–466 (2015).
10. M. B. Privitera, A. Ringer, “A CI Study in Cerebral Angiography for Product Development Strategy and Clinical Training” in *Contextual Inquiry for Medical Device Design* (Elsevier, 2015), pp. 185–210.
11. O. Kizilkilic, Vertebral artery origin stenting with buddy wire technique in tortuous subclavian artery. *Eur J Radiol* **61**, 120–123 (2007).
12. M. Goyal, G. R. Sutherland, S. Lama, P. Cimflova, N. Kashani, A. Mayank, M. N. Psychogios, L. Spelle, V. Costalat, N. Sakai, J. M. Ospel, Neurointerventional Robotics: Challenges and Opportunities. Springer [Preprint] (2020). <https://doi.org/10.1007/s00062-020-00913-2>.
13. M. J. Grundeken, X. Li, C. E. Kurpershoek, M. C. Kramer, A. Vink, J. J. Piek, J. G. P. Tijssen, K. T. Koch, J. J. Wykrzykowska, R. J. De Winter, A. C. Van Der Wal, Distal embolization of hydrophilic-coating material from Coronary guidewires after percutaneous coronary interventions. *Circ Cardiovasc Interv* **8** (2015).
14. M. E. M. K. Abdelaziz, L. Tian, M. Hamady, G. Z. Yang, B. Temelkuran, X-ray to MR: The progress of flexible instruments for endovascular navigation. IOP Publishing Ltd [Preprint] (2021). <https://doi.org/10.1088/2516-1091/ac12d6>.
15. T. M. Patel, S. C. Shah, Y. Y. Soni, R. C. Radadiya, G. A. Patel, P. O. Tiwari, S. B. Pancholy, Comparison of Robotic Percutaneous Coronary Intervention with Traditional Percutaneous Coronary Intervention: A Propensity Score-Matched Analysis of a Large Cohort. *Circ Cardiovasc Interv* **13** (2020).

16. M. Schiemann, R. Killmann, M. Kleen, N. Abolmaali, J. Finney, T. J. Vogl, Vascular guide wire navigation with a magnetic guidance system: Experimental results in a phantom. *Radiology* **232**, 475–481 (2004).
17. T. Krings, J. Finney, P. Niggemann, P. Reinacher, N. Lück, A. Drexler, J. Lovell, A. Meyer, R. Sehra, P. Schauerte, M. Reinges, F. J. Hans, A. Thron, Magnetic versus manual guidewire manipulation in neuroradiology: In vitro results. *Neuroradiology* **48**, 394–401 (2006).
18. C. Book, FDA Clears Hansen Magellan Robotic System for Peripheral Vascular Interventions, *Diagnostic and Interventional Cardiology* (2012). <https://www.dicardiology.com/product/fda-clears-hansen-magellan-robotic-system-peripheral-vascular-interventions>.
19. C. V. Riga, C. D. Bicknell, A. Rolls, N. J. Cheshire, M. S. Hamady, Robot-assisted fenestrated endovascular aneurysm repair (FEVAR) using the magellan system. *Journal of Vascular and Interventional Radiology* **24**, 191–196 (2013).
20. C. B. Beaman, N. Kaneko, P. M. Meyers, S. Tateshima, A review of robotic interventional neuroradiology. American Society of Neuroradiology [Preprint] (2021). <https://doi.org/10.3174/AJNR.A6976>.
21. A. Ali, D. H. Plettenburg, P. Breedveld, Steerable Catheters in Cardiology: Classifying Steerability and Assessing Future Challenges. IEEE Computer Society [Preprint] (2016). <https://doi.org/10.1109/TBME.2016.2525785>.
22. T. Gopesh, J. H. Wen, D. Santiago-Dieppa, B. Yan, J. S. Pannell, A. Khalessi, A. Norbash, J. Friend, Soft robotic steerable microcatheter for the endovascular treatment of cerebral disorders. *Sci Robot* **6**, eabf0601 (2021).
23. Y. Haga, Y. Muryari, T. Mineta, T. Matsunaga, H. Akahori, M. Esashi, “Small diameter hydraulic active bending catheter using laser processed super elastic alloy and silicone rubber tube” in *2005 3rd IEEE/EMBS Special Topic Conference on Microtechnology in Medicine and Biology* (2005)vol. 2005, pp. 245–248.
24. K. Ikuta, Y. Matsuda, D. Yajima, Y. Ota, “Precise bending angle control of hydraulic active catheter by pressure pulse drive” in *Proceedings - IEEE International Conference on Robotics and Automation* (2010), pp. 5588–5593.
25. A. Caenazzo, K. Althoefer, “Hypertonic saline solution for signal transmission and steering in MRI-guided intravascular catheterisation” in *Lecture Notes in Computer Science (Including Subseries Lecture Notes in Artificial Intelligence and Lecture Notes in Bioinformatics)* (Springer Verlag, 2018; [https://doi.org/10.1007/978-3-319-96728-8\\_24](https://doi.org/10.1007/978-3-319-96728-8_24))vol. 10965 LNAI, pp. 284–290.
26. C. H. Yun, L. Y. Yeo, J. R. Friend, B. Yan, Multi-degree-of-freedom ultrasonic micromotor for guidewire and catheter navigation: The NeuroGlide actuator. *Appl Phys Lett* **100**, 164101 (2012).
27. J. Sheng, X. Wang, T. M. L. Dickfeld, J. P. Desai, Towards the Development of a Steerable and MRI-Compatible Cardiac Catheter for Atrial Fibrillation Treatment. *IEEE Robot Autom Lett* **3**, 4038–4045 (2018).
28. M. Langelaar, F. Van Keulen, “Gradient-based design optimization of shape memory alloy active catheters” in *Collection of Technical Papers - AIAA/ASME/ASCE/AHS/ASC Structures, Structural Dynamics and Materials Conference* (American Institute of Aeronautics and Astronautics Inc., 2007; <http://arc.aiaa.org>)vol. 1, pp. 486–500.
29. J. H. Wiest, G. D. Buckner, Path optimization and control of a shape memory alloy actuated catheter for endocardial radiofrequency ablation. *Rob Auton Syst* **65**, 88–97 (2015).

30. T. Couture, J. Szewczyk, Design and experimental validation of an active catheter for endovascular navigation. *Journal of Medical Devices, Transactions of the ASME* **12** (2018).
31. J. H. Crews, G. D. Buckner, Design optimization of a shape memory alloy–actuated robotic catheter. *J Intell Mater Syst Struct* **23**, 545–562 (2012).
32. H. C. M. Clogenson, J. Dankelman, J. J. Van Den Dobbela, Steerable guidewire for magnetic resonance guided endovascular interventions. *Journal of Medical Devices, Transactions of the ASME* **8** (2014).
33. A. Ataollahi, R. Karim, A. S. Fallah, K. Rhode, R. Razavi, L. D. Seneviratne, T. Schaeffter, K. Althoefer, Three-degree-of-freedom MR-compatible multisegment cardiac catheter steering mechanism. *IEEE Trans Biomed Eng* **63**, 2425–2435 (2016).
34. Y. Y. Cui, C. C. Thompson, P. W. Y. Chiu, S. A. Gross, Robotics in therapeutic endoscopy (with video). Elsevier Inc. [Preprint] (2022). <https://doi.org/10.1016/j.gie.2022.05.019>.
35. J. Hwang, J. young Kim, H. Choi, A review of magnetic actuation systems and magnetically actuated guidewire- and catheter-based microrobots for vascular interventions. Springer [Preprint] (2020). <https://doi.org/10.1007/s11370-020-00311-0>.
36. S. Jeon, A. K. Hoshier, K. Kim, S. Lee, E. Kim, S. Lee, J. Y. Kim, B. J. Nelson, H. J. Cha, B. J. Yi, H. Choi, A Magnetically Controlled Soft Microrobot Steering a Guidewire in a Three-Dimensional Phantom Vascular Network. *Soft Robot* **6**, 54–68 (2019).
37. J. W. Martin, B. Scaglioni, J. C. Norton, V. Subramanian, A. Arezzo, K. L. Obstein, P. Valdastrì, Enabling the future of colonoscopy with intelligent and autonomous magnetic manipulation. *Nat Mach Intell* **2**, 595–606 (2020).
38. Q. Boehler, S. Gervasoni, S. L. Charreyron, C. Chautems, B. J. Nelson, On the Workspace of Electromagnetic Navigation Systems. *IEEE TRANSACTIONS ON ROBOTICS* **39**, 791–807 (2023).
39. J. Bradfield, R. Tung, R. Mandapati, N. G. Boyle, K. Shivkumar, Catheter ablation utilizing remote magnetic navigation: A review of applications and outcomes. *Pacing Clin Electrophysiol* [Preprint] (2012). <https://doi.org/10.1111/j.1540-8159.2012.03382.x>.
40. G. Dabus, R. J. Gerstle, D. W. T. Cross, C. P. Derdeyn, C. J. Moran, Neuroendovascular magnetic navigation: Clinical experience in ten patients. *Neuroradiology* **49**, 351–355 (2007).
41. Y. Kim, E. Genevriere, P. Harker, J. Choe, M. Balicki, R. W. Regenhardt, J. E. Vranic, A. A. Dmytriw, A. B. Patel, X. Zhao, Telerobotic neurovascular interventions with magnetic manipulation. *Sci Robot* **7** (2022).
42. K. Lock, “Stereotaxis Genesis RMN with Navigant Workstation (NWS) and Cardiodrive System (Genesis MNS) , K193147” (St. Louis, MO, 2020); [https://www.accessdata.fda.gov/cdrh\\_docs/pdf19/K193147.pdf](https://www.accessdata.fda.gov/cdrh_docs/pdf19/K193147.pdf).
43. Stereotaxis Inc., “Genesis Robotic Magnetic Navigation System™ with Stereotaxis Imaging Model S Fluoroscope Site Planning Considerations” (St. Louis, MO, 2019); <https://www.roboticep.com/toolkit/PlanningGuides/PRO-1024-Genesis-RMN-Magnetic-Navigation-System-with-Stereotaxis-Imaging.pdf>.
44. G. G. Tóth, M. Yamane, G. R. Heyndrickx, How to select a guidewire: technical features and key characteristics. *Heart* **101**, 645–652 (2015).
45. M. E. M. K. Abdelaziz, L. Tian, M. Hamady, G. Z. Yang, B. Temelkuran, X-ray to MR: The progress of flexible instruments for endovascular navigation. IOP Publishing Ltd [Preprint] (2021). <https://doi.org/10.1088/2516-1091/ac12d6>.
46. P. M. Meyers, H. C. Schumacher, K. Tanji, R. T. Higashida, L. R. Caplan, Use of stents to treat intracranial cerebrovascular disease. *Annu Rev Med* [Preprint] (2007). <https://doi.org/10.1146/annurev.med.58.121205.100631>.

47. R. Dreyfus, Q. Boehler, C. Chautems, B. J. Nelson, “A navigation console to steer magnetic instruments under radiological guidance for neuro-vascular interventions” in *Proceedings of The 14th Hamlyn Symposium on Medical Robotics 2022* (The Hamlyn Centre, Imperial College London London, UK, 2022; <https://hamlynsymposium.org/proceedings/>), pp. 79–80.
48. M. Quigley, K. Conley, B. P. Gerkey, J. Faust, T. Foote, J. Leibs, R. Wheeler, A. Y. Ng, *ROS: An Open-Source Robot Operating System* (ICRA, 2009).
49. A. T. Rai, J. P. Hogg, B. Cline, G. Hobbs, Cerebrovascular geometry in the anterior circulation: An analysis of diameter, length and the vessel taper. *J Neurointerv Surg* **5**, 371–375 (2013).
50. J. Lussi, S. Gervasoni, M. Mattille, R. Dreyfus, Q. Boehler, M. Reinehr, N. Ochsenbein, B. J. Nelson, U. Moehrlen, Magnetically Guided Laser Surgery for the Treatment of Twin-to-Twin Transfusion Syndrome. *Advanced Intelligent Systems* **4**, 2200182 (2022).
51. Q. Boehler, S. Gervasoni, S. L. Charreyron, C. Chautems, B. J. Nelson, On the Workspace of Electromagnetic Navigation Systems. doi: 10.24433/CO.2090933.v1.
52. J. Y. Chueh, A. K. Wakhloo, M. J. Gounis, Neurovascular modeling: Small-batch manufacturing of silicone vascular replicas. *American Journal of Neuroradiology* **30**, 1159–1164 (2009).
53. M. Sidiq, E. Scheidecker, A. Potreck, U. Neuberger, C. S. Weyland, S. Mundiyanapurath, M. Bendszus, M. A. Möhlenbruch, F. Seker, Aortic Arch Variations and Supra-aortic Arterial Tortuosity in Stroke Patients Undergoing Thrombectomy: Retrospective Analysis of 1705 Cases. *Clin Neuroradiol*, 1–8 (2022).
54. Double-Wire Technique for Giant Cerebral Aneurysms - Endovascular Today. <https://evtoday.com/articles/2011-feb/double-wire-technique-for-giant-cerebral-aneurysms>.
55. J. Burel, J. Cornacchini, M. Garnier, S. Patrier, A. Guigné, E. Gerardin, C. Papagiannaki, N. Sourour, E. Shotar, K. Premat, C. Laporte, F. Clarençon, The human placenta as a model for training and research in mechanical thrombectomy: Clarifications and use of the chorionic plate veins. *Front Neurol* **13** (2022).
56. J. C. K. Kwok, W. Huang, W. C. Leung, S. K. Chan, K. Y. Chan, K. M. Leung, A. C. H. Chu, A. K. N. Lam, Human placenta as an ex vivo vascular model for neurointerventional research. *J Neurointerv Surg* **6**, 394–399 (2014).
57. J. Edwards, H. Abdou, N. Patel, M. J. Madurska, K. Poe, J. E. Bonin, M. J. Richmond, T. E. Rasmussen, J. J. Morrison, The functional vascular anatomy of the swine for research. SAGE Publications Ltd [Preprint] (2022). <https://doi.org/10.1177/1708538121996500>.
58. R. Dreyfus, Q. Boehler, B. J. Nelson, A Simulation Framework for Magnetic Continuum Robots. *IEEE Robot Autom Lett* **7**, 8370–8376 (2022).
59. S. Mishra, Language of CTO interventions – Focus on hardware. Elsevier B.V. [Preprint] (2016). <https://doi.org/10.1016/j.ihj.2016.06.015>.
60. T. Beyna, M. Arvanitakis, M. Schneider, C. Gerges, J. Hoellerich, J. Devière, H. Neuhaus, Total motorized spiral enteroscopy: first prospective clinical feasibility trial. *Gastrointest Endosc* **93**, 1362–1370 (2021).
61. B. Purushottam, P. Krishnan, “Novel Technique to Cross Infrapopliteal Artery Chronic Total Occlusions” (2020).
62. M. Egred, Usefulness of the Turnpike Gold Catheter in Balloon Uncrossable Coronary Lesions. *Clinical Cardiology and Cardiovascular Interventions* **3**, 01–07 (2020).
63. K. Ishiyama, K. I. Arai, M. Sendoh, A. Yamazaki, “Spiral-type micro-machine for medical applications” in *MHS2000. Proceedings of 2000 International Symposium on Micromechatronics and Human Science (Cat. No.00TH8530)20* (IEEE, 2000; <http://ieeexplore.ieee.org/document/903292/>), pp. 65–69.

64. T. Wang, H. Ugurlu, Y. Yan, M. Li, M. Li, A.-M. Wild, E. Yildiz, M. Schneider, D. Sheehan, W. Hu, M. Sitti, Adaptive wireless millirobotic locomotion into distal vasculature. *Nat Commun* **13**, 4465 (2022).
65. B. J. Nelson, I. K. Kaliakatsos, J. J. Abbott, Microrobots for Minimally Invasive Medicine. *Annu Rev Biomed Eng.* **12**, 55–85 (2010).
66. F. Ullrich, F. Qiu, J. Pokki, T. Huang, S. Pane, B. J. Nelson, “Swimming characteristics of helical microrobots in fibrous environments” in *Proceedings of the IEEE RAS and EMBS International Conference on Biomedical Robotics and Biomechatronics* (IEEE Computer Society, 2016)vols. 2016-July, pp. 470–475.
67. A. Hosney, A. Klingner, S. Misra, I. S. M. Khalil, “Propulsion and steering of helical magnetic microrobots using two synchronized rotating dipole fields in three-dimensional space” in *IEEE International Conference on Intelligent Robots and Systems* (Institute of Electrical and Electronics Engineers Inc., 2015)vols. 2015-December, pp. 1988–1993.
68. W. Lee, S. Jeon, J. Nam, G. Jang, Dual-body magnetic helical robot for drilling and cargo delivery in human blood vessels. *J Appl Phys* **117**, 17B314 (2015).
69. A. C. Bakenecker, A. von Gladiss, H. Schwenke, A. Behrends, T. Friedrich, K. Lüdtke-Buzug, A. Neumann, J. Barkhausen, F. Wegner, T. M. Buzug, Navigation of a magnetic micro-robot through a cerebral aneurysm phantom with magnetic particle imaging. *Sci Rep* **11**, 14082 (2021).
70. J. Sa, J. Park, E. Jung, N. Kim, D. Lee, S. Bae, Y. Lee, G. Jang, Separable and Recombinable Magnetic Robot for Robotic Endovascular Intervention. *IEEE Robot Autom Lett* **8**, 1881–1888 (2023).
71. S. Lee, S. Lee, S. Kim, C. H. Yoon, H. J. Park, J. Y. Kim, H. Choi, Fabrication and Characterization of a Magnetic Drilling Actuator for Navigation in a Three-dimensional Phantom Vascular Network. *Sci Rep* **8**, 3691 (2018).
72. J. Leclerc, H. Zhao, D. Bao, A. T. Becker, In Vitro Design Investigation of a Rotating Helical Magnetic Swimmer for Combined 3-D Navigation and Blood Clot Removal. *IEEE Transactions on Robotics*, 1–8 (2022).
73. I. S. M. Khalil, D. Mahdy, A. El Sharkawy, R. R. Moustafa, A. F. Tabak, M. E. Mitwally, S. Hesham, N. Hamdi, A. Klingner, A. Mohamed, M. Sitti, Mechanical Rubbing of Blood Clots Using Helical Robots under Ultrasound Guidance. *IEEE Robot Autom Lett* **3**, 1112–1119 (2018).
74. I. S. M. Khalil, A. F. Tabak, K. Sadek, D. Mahdy, N. Hamdi, M. Sitti, Rubbing Against Blood Clots Using Helical Robots: Modeling and in Vitro Experimental Validation. *IEEE Robot Autom Lett* **2**, 927–934 (2017).
75. D. Mahdy, R. Reda, N. Hamdi, I. S. M. Khalil, Ultrasound-guided minimally invasive grinding for clearing blood clots: Promises and challenges. *IEEE Instrum Meas Mag* **21**, 10–14 (2018).
76. C.-H. Yu, S. H. Kim, Multifunctional Robotic Guidewire System using Spiral-type Magnetic Microrobot with Magnetic Manipulation. *Journal of Magnetism* **21**, 616–621 (2016).
77. A. J. Sperry, T. J. Schwehr, E. K. Pinegar, O. B. Richards, J. D. Rolston, M. D. Alexander, B. Coats, J. J. Abbott, A. Kuntz, Screw-tip Soft Magnetically Steerable Needles. *IEEE Trans Med Robot Bionics*, doi: 10.1109/TMRB.2023.3265721 (2023).
78. X. Jin, S. Guo, J. Guo, P. Shi, T. Tamiya, H. Hirata, Development of a Tactile Sensing Robot-Assisted System for Vascular Interventional Surgery. *IEEE Sens J* **21**, 12284–12294 (2021).
79. V. M. Pereira, N. M. Cancelliere, P. Nicholson, I. Radovanovic, K. E. Drake, J. M. Sungur, T. Krings, A. Turk, First-in-human, robotic-assisted neuroendovascular intervention. *J Neurointerv Surg* **12**, 338–340 (2020).

80. G. W. Britz, J. Tomas, A. Lumsden, Feasibility of Robotic-Assisted Neurovascular Interventions: Initial Experience in Flow Model and Porcine Model. *Clin Neurosurg* **86**, 309–314 (2020).
81. M. Razban, J. Dargahi, B. Boulet, “A Sensor-less Catheter Contact Force Estimation Approach in Endovascular Intervention Procedures” in *IEEE International Conference on Intelligent Robots and Systems* (Institute of Electrical and Electronics Engineers Inc., 2018), pp. 2100–2106.
82. Z. Yang, L. Yang, M. Zhang, Q. Wang, C. H. Simon, L. Zhang, Magnetic Control of a Steerable Guidewire under Ultrasound Guidance Using Mobile Electromagnets. *IEEE Robot Autom Lett* **6**, 1280–1287 (2021).
83. K. R. J. Chun, E. Wissner, B. Koektuerk, M. Konstantinidou, B. Schmidt, T. Zerm, A. Metzner, R. Tilz, S. Boczor, A. Fuernkranz, F. Ouyang, K. H. Kuck, Remote-controlled magnetic pulmonary vein isolation using a new irrigated-tip catheter in patients with atrial fibrillation. *Circ Arrhythm Electrophysiol* **3**, 458–464 (2010).
84. M. Mattmann, C. De Marco, F. Briatico, S. Tagliabue, A. Colusso, X. Z. Chen, J. Lussi, C. Chautems, S. Pané, B. Nelson, Thermoset Shape Memory Polymer Variable Stiffness 4D Robotic Catheters. *Advanced Science* **9** (2022).
85. Y. Kim, G. A. Parada, S. Liu, X. Zhao, Ferromagnetic soft continuum robots. *Sci Robot* **4**, eaax7329 (2019).
86. S. Zhang, M. Yin, Z. Lai, C. Huang, C. Wang, W. Shang, X. Wu, Y. Zhang, T. Xu, Design and Characteristics of 3D Magnetically Steerable Guidewire System for Minimally Invasive Surgery. *IEEE Robot Autom Lett* **7**, 4040–4046 (2022).
87. K. O’Donoghue, P. Cantillon-Murphy, Deflection modeling of permanent magnet spherical chains in the presence of external magnetic fields. *J Magn Magn Mater* **343**, 251–256 (2013).
88. A. Hong, Q. Boehler, R. Moser, A. Zemmar, L. Stieglitz, B. J. Nelson, 3D path planning for flexible needle steering in neurosurgery. *The International Journal of Medical Robotics and Computer Assisted Surgery* **15**, e1998 (2019).
89. G. Pittiglio, M. Mencattelli, P. E. Dupont, “Closed-form Kinematic Model and Workspace Characterization for Magnetic Ball Chain Robots” in *2023 International Symposium on Medical Robotics (ISMR)* (2023), pp. 1–7.
90. G. Pittiglio, P. Lloyd, T. Da Veiga, O. Onaizah, C. Pompili, J. H. Chandler, P. Valdastrì, Patient-Specific Magnetic Catheters for Atraumatic Autonomous Endoscopy. *Soft Robot* **9**, 1120–1133 (2022).
91. L. Karstensen, J. Ritter, J. Hatzl, F. Ernst, J. Langejürgen, C. Uhl, F. Mathis-Ullrich, Recurrent neural networks for generalization towards the vessel geometry in autonomous endovascular guidewire navigation in the aortic arch. *Int J Comput Assist Radiol Surg*, 1–10 (2023).
92. P. M. Scheikl, B. Gyenes, R. Younis, C. Haas, G. Neumann, M. Wagner, F. Mathis-Ullrich, LapGym -- An Open Source Framework for Reinforcement Learning in Robot-Assisted Laparoscopic Surgery. *arXiv e-prints* (2023).
93. L. Karstensen, J. Ritter, J. Hatzl, T. Pätz, J. Langejürgen, C. Uhl, F. Mathis-Ullrich, Learning-based autonomous vascular guidewire navigation without human demonstration in the venous system of a porcine liver. *Int J Comput Assist Radiol Surg*, 1–8 (2022).
94. P. Schegg, J. Dequidt, E. Coevoet, E. Leurent, R. Sabatier, P. Preux, C. Duriez, “Automated Planning for Robotic Guidewire Navigation in the Coronary Arteries” in *2022 IEEE 5th International Conference on Soft Robotics, RoboSoft 2022* (Institute of Electrical and Electronics Engineers Inc., 2022), pp. 239–246.
95. G. Z. Yang, J. Cambias, K. Cleary, E. Daimler, J. Drake, P. E. Dupont, N. Hata, P. Kazanzides, S. Martel, R. V. Patel, V. J. Santos, R. H. Taylor, Medical robotics-



- Regulatory, ethical, and legal considerations for increasing levels of autonomy. American Association for the Advancement of Science [Preprint] (2017).  
<https://doi.org/10.1126/scirobotics.aam8638>.
96. A. Attanasio, B. Scaglioni, E. De Momi, P. Fiorini, P. Valdastri, Autonomy in Surgical Robotics. *Annu Rev Control Robot Auton Syst* **4**, 651–679 (2021).
  97. P. E. Dupont, B. J. Nelson, M. Goldfarb, B. Hannaford, A. Menciassi, M. K. O'Malley, N. Simaan, P. Valdastri, G. Z. Yang, A decade retrospective of medical robotics research from 2010 to 2020. American Association for the Advancement of Science [Preprint] (2021).  
<https://doi.org/10.1126/scirobotics.abi8017>.
  98. A. J. Petruska, J. Edelmann, B. J. Nelson, Model-Based Calibration for Magnetic Manipulation. *IEEE Trans Magn* **53** (2017).
  99. K. Takashima, R. Shimomura, T. Kitou, H. Terada, K. Yoshinaka, K. Ikeuchi, Contact and friction between catheter and blood vessel. *Tribol Int* **40**, 319–328 (2007).
  100. T. M. Bydlon, A. Torjesen, S. Fokkenrood, A. Di Tullio, M. L. Flexman, 3D Visualisation of Navigation Catheters for Endovascular Procedures Using a 3D Hub and Fiber Optic RealShape Technology: Phantom Study Results. *EJVES Vasc Forum* **59**, 24–30 (2023).

### **Acknowledgments:**

The authors acknowledge support from the European Union's Horizon 2020 research and innovation programme under grant agreement No 952152, project ANGIE (MAGnetically steerable wireless Nanodevices for the tarGeted delivery of therapeutIc agents in any vascular rEgion of the body). Furthermore, the authors thank Prof. Frédéric Clarençon from the Department of Neuroradiology at the Pitié-Salpêtrière Hospital in Paris, France for sharing his knowledge of the placenta preparation.

### **Funding:**

Swiss National Science Foundation grant 200020B\_185039 (RD, QB)  
ERC Advanced grant Soft Micro Robotics (SOMBOT) 743217 (RD, SL, SG, JL)  
ITC-InnoHK grant 16312 (RD, QB, SL)

### **Author contributions:**

Conceptualization: RD, QB, SL, BN  
Methodology: RD, QB, SL, PG, JB  
Software: RD, QB, SG  
Validation: RD, JL, DS  
Formal analysis: RD  
Investigation: RD, SL, JL, SG, DS  
Resources: SG, PG, JB, MM, LR, NO, MR  
Data Curation: RD, DS  
Writing - Original Draft: RD, SL  
Writing - Review & Editing: RD  
Visualization: RD  
Supervision: BN  
Project administration: QB, CC, LR  
Funding acquisition: QB, CC, BN

### **Competing interests:**

RD, SL, CC and BN are authors on patent application EP22182617 “Magnetically steerable device for use inside of a mammalian body” covering the presented helical device.

RD, SL and BN are authors on patent application EP22177147 “Steerable device for use inside of a mammalian body” describing the magnetic articulating tip technology.

CC is chief technology officer and co-founder, and BN is mentor and co-founder of the company Nanoflex Robotics AG, Zurich, Switzerland.

BN is the chief scientific advisor of *Science Robotics*.

**Data availability statement:**

All data needed to evaluate the conclusions in this paper are present in the paper or the Supplementary Materials. The data and codes for this study have been deposited in the database [10.3929/ethz-b-000651465](https://doi.org/10.3929/ethz-b-000651465).

## Figure captions

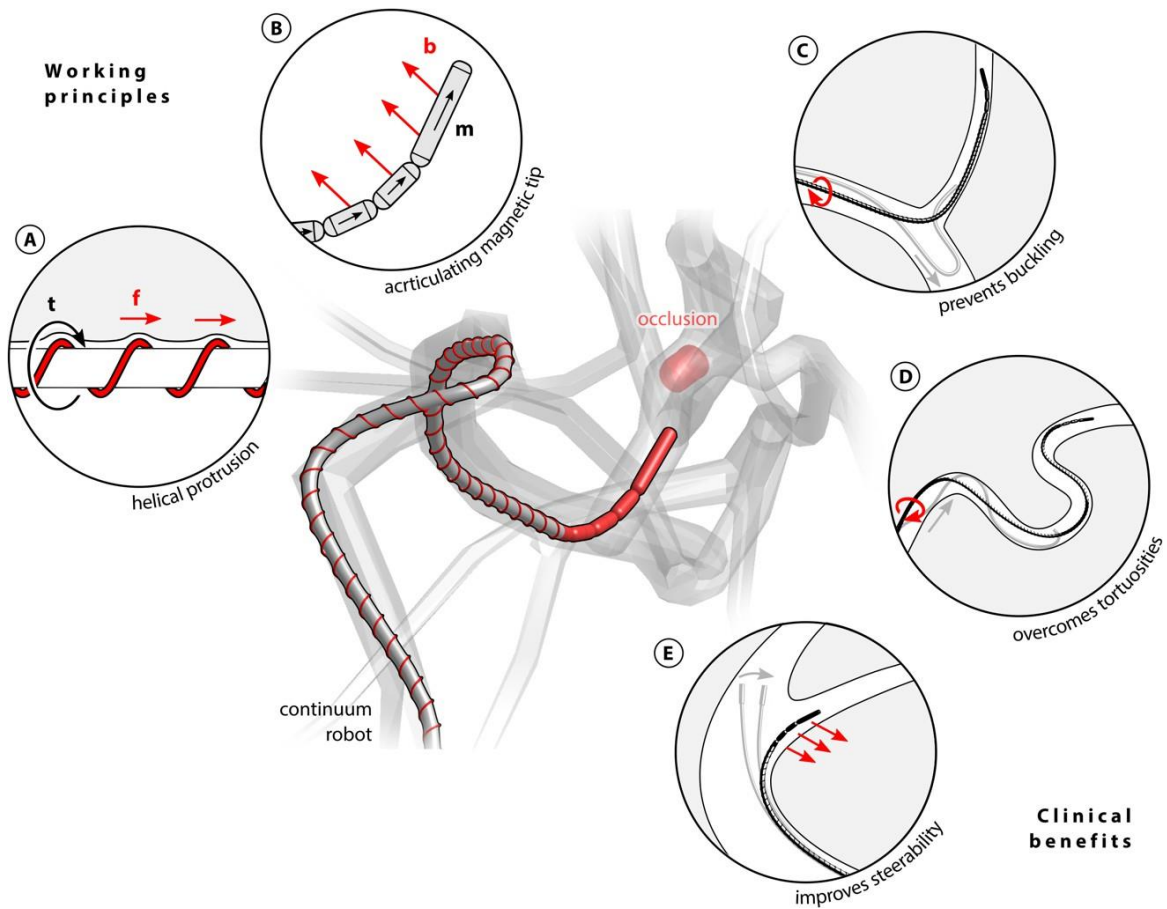


**Fig. 1. Helical magnetic continuum robot with articulated magnetic tip.** (A) The helical protrusion on the outer surface of the continuum robot, upon rotation, pushes the robot tip forward. (B) The segmented articulating magnetic tip increases the magnetic volume and decreases bending stiffness for improved steerability. (C) The helical robot prevents buckling and (D) overcomes tortuous vessels. (E) The articulating tip allows for large tip deflections.

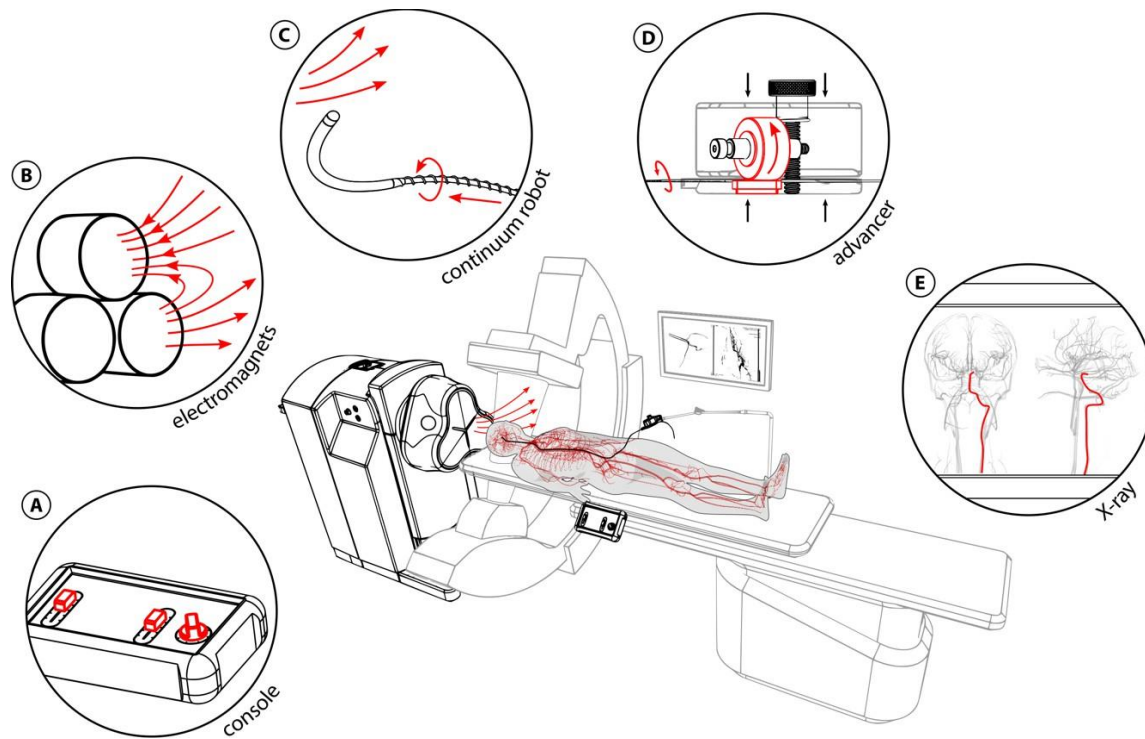


**Fig. 2. Robotic system overview.** (A) The console takes user inputs to control the magnetic field direction and insertion speed. (B) The electromagnets of the eMNS generate the external magnetic fields used to steer the magnetic devices inside the patient. (C) The helical magnetic endovascular device. (D) The motorized advancer unit pushes and rotates the helical magnetic devices. (E) The X-ray image provides visual feedback of the vasculature and the magnetic device.

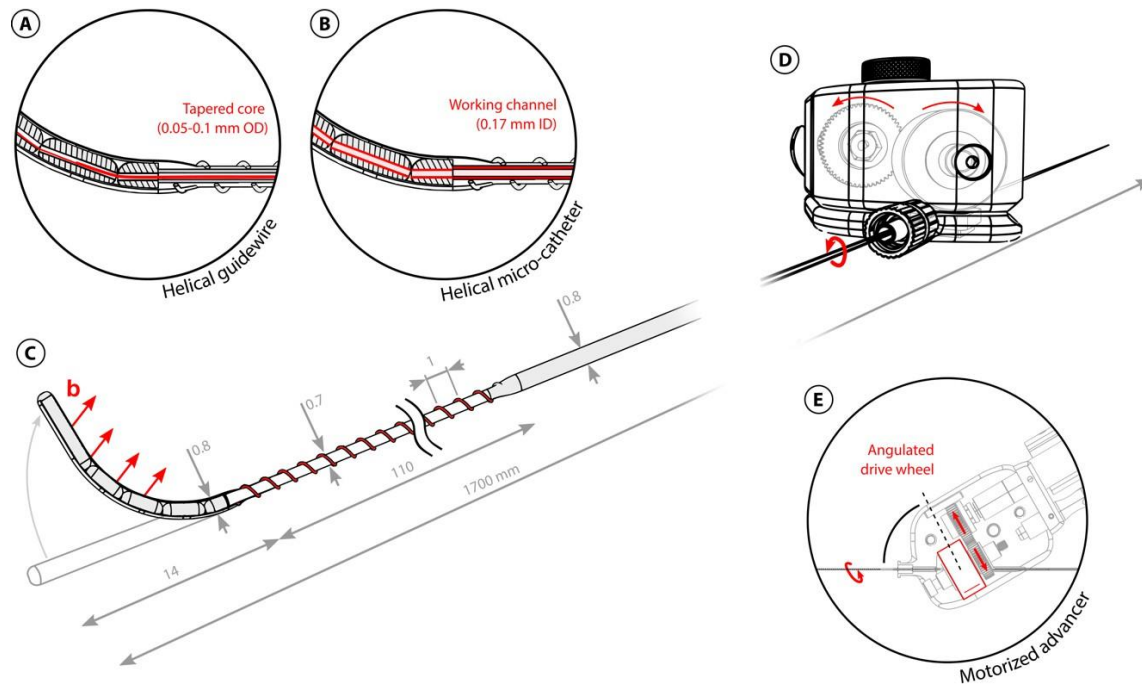


**Fig. 3. Helical magnetic continuum robot (mCR) and advancer design.** (A) A magnified view of the guidewire helical mCR with a tapered nitinol core (red) for stiffness optimization. (B) A magnified view of the microcatheter helical mCR with working channel (red) for fluid injection. (C) The helical mCR has a flexible, magnetic tip with articulating links and a helical protrusion on its outer surface. (D) The advancer unit actuates the helical mCR by translation and rotation. (E) The roller axis of the motorized advancer is tilted to push and rotate the helical mCR.

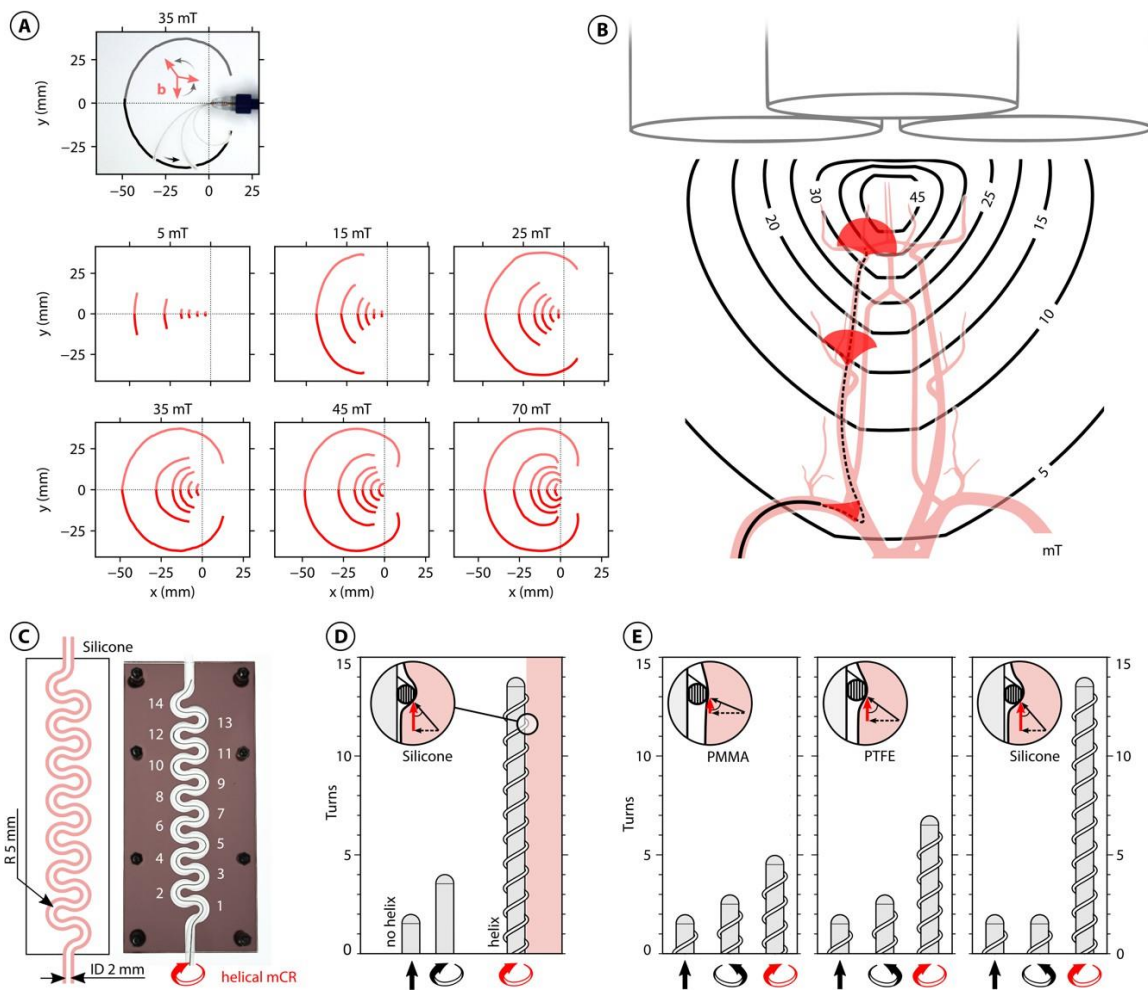


**Fig. 4. Workspace and helix effectiveness measurement of the helical magnetic continuum robot.** (A) A sweep of parameters and tip tracking reveal the reachable workspace at different magnetic field magnitudes. (B) The mCR reachable workspace when navigating the supraaortic arteries and actuated by a three-coiled eMNS. (C) The flat vessel model with interchangeable lumen material: polymethyl methacrylate (PMMA), polytetrafluorethylene (PTFE) and silicone. (D) The comparison between a helical device actuated by rotation in a clockwise direction and a device without helical protrusion, actuated by translation and rotation. The helix engages with the soft material and when rotated, generates a forward pushing force. (E) The helix effectiveness: the continuum robot is inserted as far as possible into three tortuous vessel models with three different materials for different engagement levels (PMMA, PTFE, and silicone). For each model, the mCR is inserted in three ways, first by pushing only, then whilst rotating counterclockwise, and finally whilst rotating clockwise.

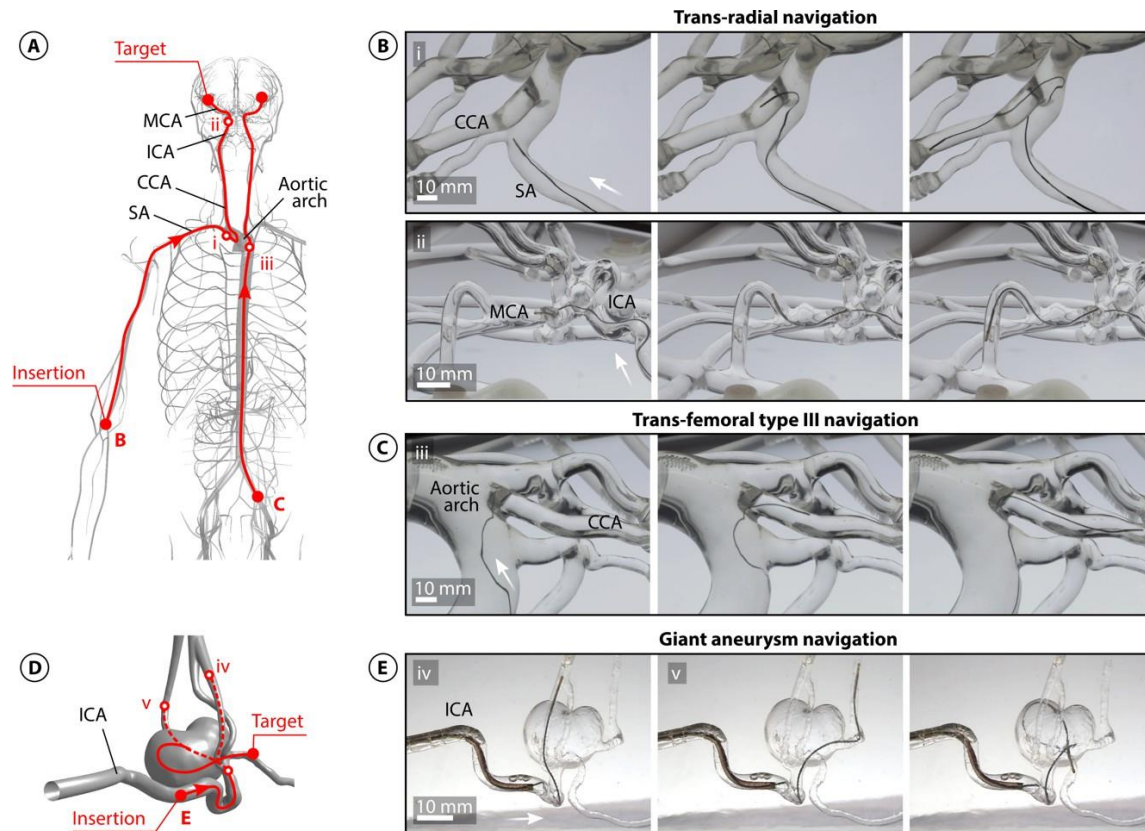


**Fig. 5. In vitro navigation.** (A) An overview of the human vasculature with insertion points in the radial (B) and femoral arteries (C), and target in the cerebral arteries. (B) The navigation in distal cerebral vessels through the trans-radial approach in a silicone model, starting from the subclavian artery (SA), into the common carotid artery (CCA), across the internal carotid artery (ICA), to the middle cerebral artery (MCA)-M2 segment. (C) The navigation across a type III aortic arch through the trans-femoral approach access of a silicone model. (D) An overview of the navigation in a fusiform giant aneurysm with insertion through a catheter in the internal carotid artery (E). (E) The navigation along the parent vessels in a fusiform giant aneurysm situation in a silicone model.

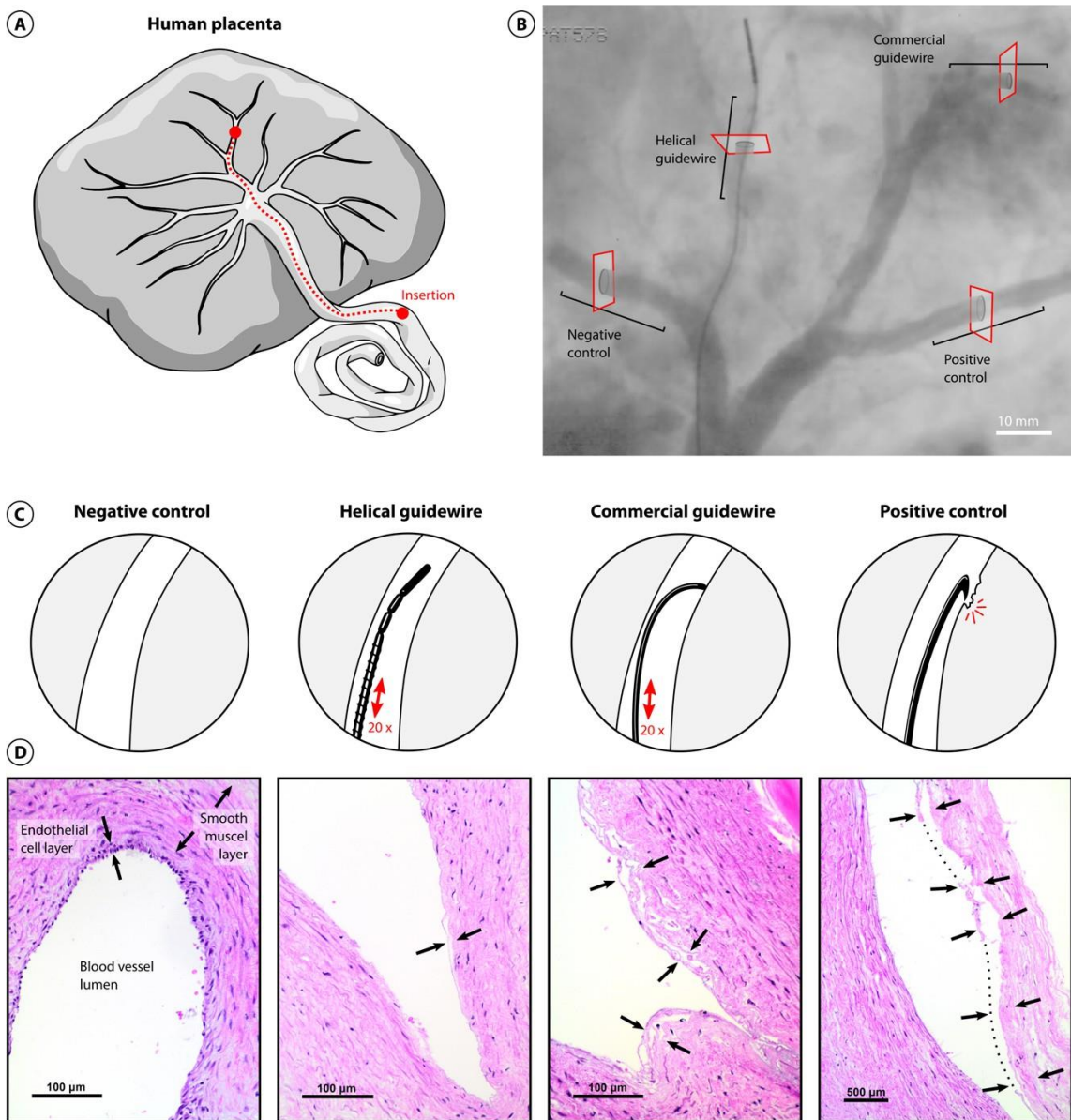


**Fig. 6. Histological analysis of human placenta blood vessels.** (A) An illustration of a human placenta with device insertion point. Ex vivo placenta veins are utilized for endoluminal device testing because they are similar to human brain arteries. (B) For comparison, different devices (negative and positive controls, as well as helical and commercial guidewires) were inserted into individual blood vessels. After navigation, histological analysis was performed on multiple sections (example slices are indicated in red) which were extracted from samples taken from various locations (examples are indicated by black lines). (C) The negative control is a blood vessel that was left untouched whereas the positive control consists of an intentionally damaged vessel using a sharp wire tool. The helical and commercial guidewires were inserted and retracted twenty times. (D) Example images of the histological analysis reveal the physical impact on the endothelial cell layer and inner vessel wall. The black arrows indicates minor cell layer detachments (helical and commercial guidewire) and more extensive laceration of the endothelial cell layer (positive control). The black dotted line indicates the torn and missing cell layer.



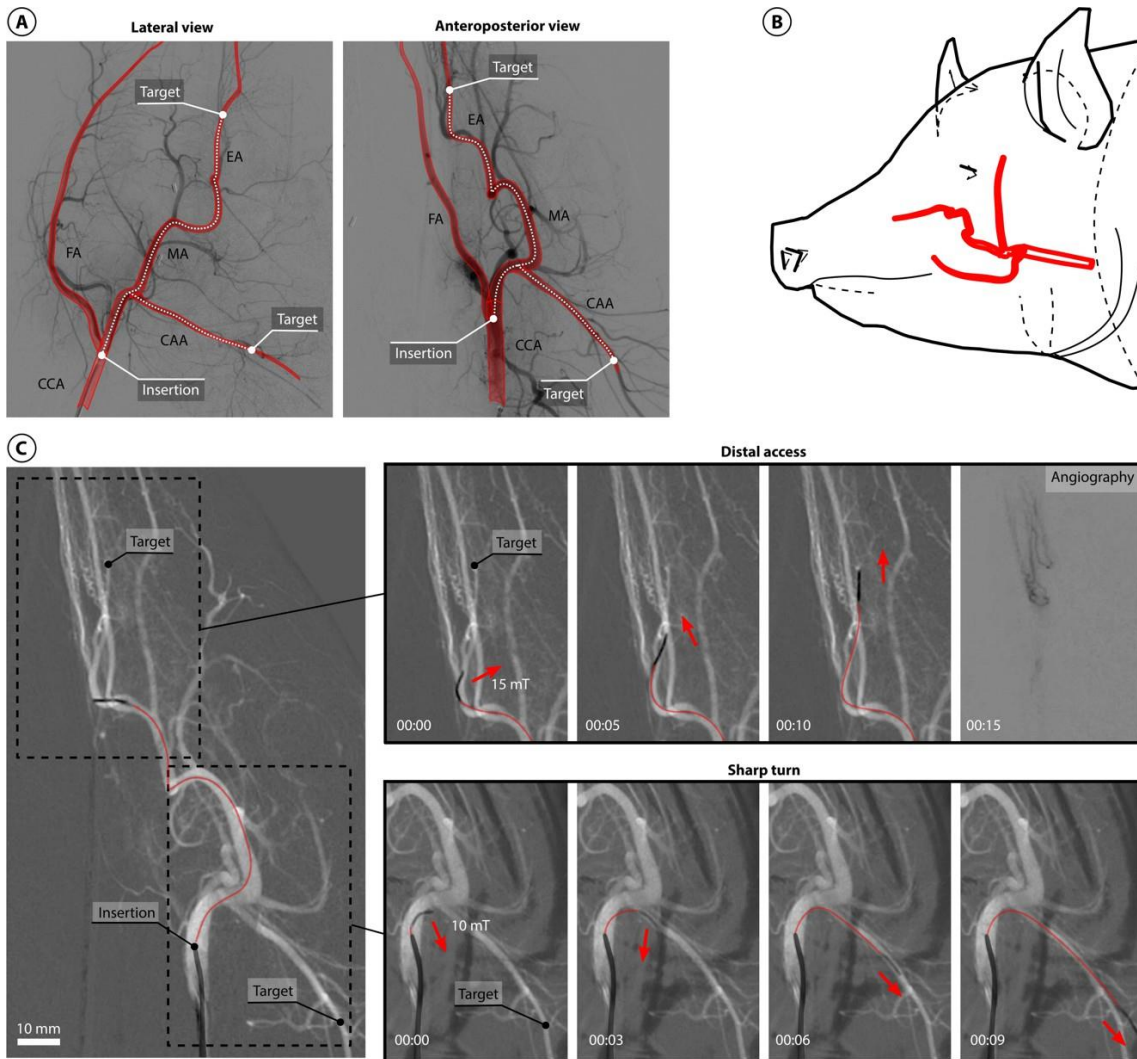


**Fig. 7. In vivo navigation.** (A) The lateral and anteroposterior view of the pig's vascular anatomy (legend: caudal auricular artery (CAA), common carotid artery (CCA), ethmoidal artery (EA), facial artery (FA), maxillary artery (MA)). (B) The 3D representation of the pig's vascular anatomy. (C) The in vivo navigation in millimeter-sized vessels with injection of contrast agent (angiography) and steering at low magnetic fields (10mT), with over 90° turn.

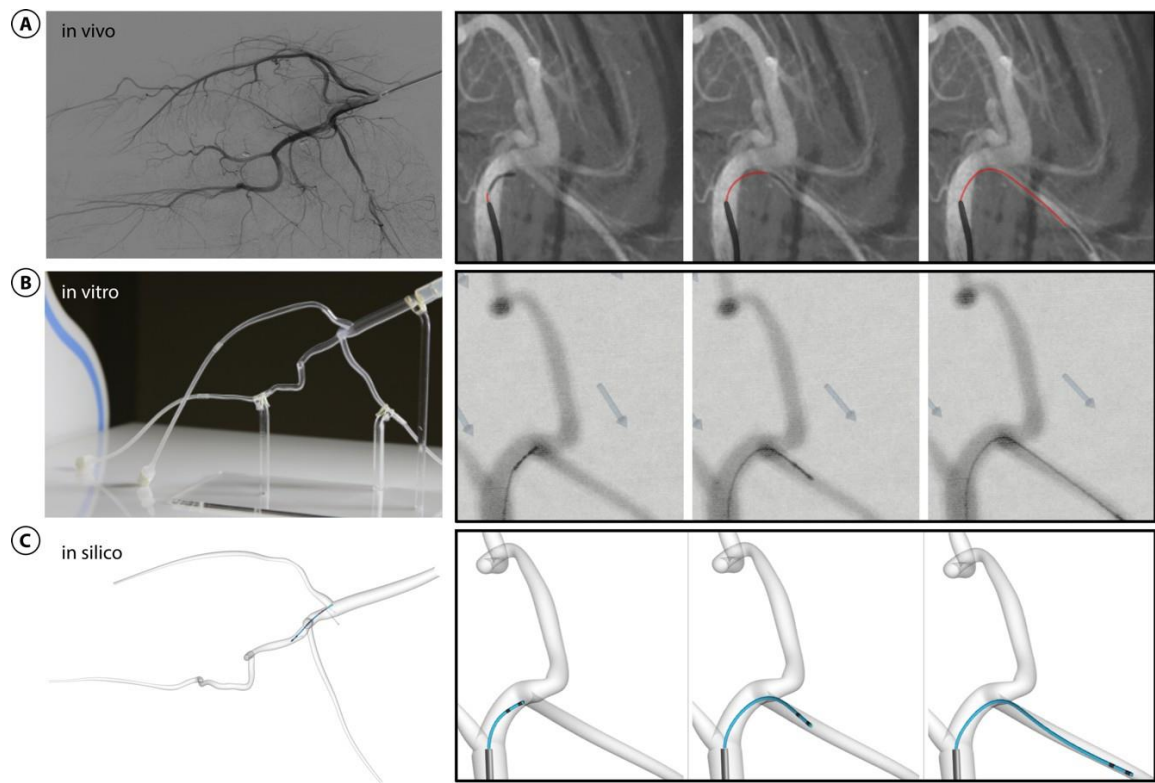


**Fig. 8. Side-by-side comparison of in vivo, in vitro, and in silico navigation.** (A) The in vivo navigation. It serves as a ground truth for the simulated navigations. (B) The in vitro navigation. (C) The in silico navigation.

## Supplementary Materials

### Supplementary Methods:

#### Analytical formulation of helix pushing force

The axial pushing force generated by the helix  $F_{hel}$  can be expressed analytically by the screw equation, assuming there is contact with the vessel wall (see fig. S3).

$$F_{hel} = T_{hel} \cdot \frac{2 \pi D - \mu L \sec(\lambda)}{D L + \pi \mu D \sec(\lambda)} \quad (S1)$$

The helix force is directly proportional to the externally applied driving torque  $T_{hel}$  and further depends on the mean helix diameter  $D$ , the helix pitch length  $L$ , the friction coefficient  $\mu$  and the angle  $\lambda$ . The angle  $\lambda$  is the angle between the axis and the normal force acting on the helix when the helix engages with the vessel wall: in a soft material, the engagement angle will be small whereas in a hard material, the engagement angle will be large (see Fig. 4E and fig. S3D). Equation S1 applies in a regime where there is perfect engagement with no slippage. Once the helix force exceeds a certain force  $F_{slip}$  the helix will start to slip or deform the vessel. This occurs when there is insufficient linear translation per revolution. One instance where this can occur is during the buckling of the mCR. In this scenario, despite the rotation of the device, the linear translation is not efficiently transmitted to the distal section. Consequently, the helix in the distal section rotates without advancing by one pitch length per revolution, ultimately leading to slippage. Because of the high nonlinearity of this regime, we simplify  $F_{hel}$  with

$$F_{hel} = F_{slip}, \quad (S2)$$

where an approximation of  $F_{slip}$  is estimated experimentally.

#### Design parameters of the helical magnetic continuum robot

The parameters of the helical mCR were determined as follows:

Considering equation S1, the helix pushing force  $F_{hel}$  is large when the pitch length  $L$  is small. Therefore, the pitch length should be as short as possible. However, there is a limit to which the pitch length can be reduced, as the speed of rotation increases when the pitch decreases. We chose a speed of one revolution per millimeter of advancement, which corresponds to a 1 mm pitch length.

Furthermore, the engagement deteriorates if the helix wires are too close because there is insufficient space between the wires to deform the vessel wall. The quality of the engagement is characterized by the engagement angle  $\lambda$  (see Fig. 4E and fig. S3D). The helix is more effective if the engagement angle is small. In the most extreme cases, the wires touch, which leads to zero engagement. To increase the quality of the engagement, one can increase the helix wire diameter. Given that the maximum outer diameter is limited, we tried to increase the helix wire diameter by decreasing the backbone diameter while maintaining a sufficiently large lumen inner diameter. However, this reduces the wall thickness, which

decreases the torquability of the device. Regarding the outer diameter, our aim was to create a device that can navigate the millimeter-sized cranial arteries and fit inside a 5 Fr (1.7 mm) guiding catheter. This requirement determined the maximum outer diameter, which had to be below 1 mm. Balancing all these requirements, we found a feasible design of 0.7 mm helix outer diameter, 0.1 mm helix wire outer diameter, 0.5 mm backbone outer diameter, and 0.17 lumen inner diameter. 316 stainless steel was chosen for the material of the backbone and the helix because of its torque-transmitting properties and biocompatibility. For comparison, polymer or nitinol fillers would have been biocompatible but would have been too elastic for effective torque transition.

Overall, many of the design choices were driven by a combination of theoretical and practical considerations. This approach allowed us to construct a highly effective device tailored to the specific requirements of the intended task of navigating tortuous millimeter-sized blood vessels.

### Setup of the ex vivo human placenta study

Human placentas were procured with written consent and approval from the Ethical Committee of the District of Zürich (BASEC-Nr. 2023-00110). The placentas were prepared following the protocol described in (55) with an injection of 50 volume percentage contrast agent (Ultravist, Iopromid, Bayer Vital GmbH, Germany) saline solution for enhanced visibility under X-ray imaging. Imaging was performed with a mono-plane angiography system (Allura Xper FD20 fluoroscope, Philips N.V., Amsterdam, Netherlands). The commercial guidewire and the positive control device were inserted manually by hand, whereas the helical guidewire was magnetically steered. The whole placenta was fixed in 4% paraformaldehyde for 48 hours. Then representative tissue sections were removed and then processed according to the standards of routine histopathological diagnosis of the Department of Pathology and Molecular Pathology (University Hospital of Zurich). Briefly, the fixed tissue sections were embedded in paraffin, cut into 2–3  $\mu\text{m}$  thick sections, then stained with standard hematoxylin and eosin stain. For each condition shown in Fig. 6C (negative control, helical guidewire, commercial guidewire, and positive control), samples were extracted from two distinct locations, from which two blocks were obtained and subsequently divided into 8 sections each. An expert pathologist then evaluated these sections in a blind test setup. Fig. 6B provides a visual representation of one sample and one slice for each condition. The histological images in Fig. 6D are selected examples chosen by the pathologist.

### Simulation of the helical magnetic continuum robot

The mCR was simulated with the dynamic FEM based simulation described in (58). An illustration of the simulation principle can be seen in fig. S3. The simulation was temporally discretized with timestep  $dt$ . At every timestep a collision detection pipeline first detected and handled collisions, then a physical solver solved the ordinary differential equations (ODEs), and lastly, the system was updated. The physical solver uses an implicit Euler method to solve the ODEs:

$$\mathbf{H}\mathbf{M} + dt \frac{\partial \mathbf{f}}{\partial \mathbf{v}} + dt^2 \frac{\partial \mathbf{f}}{\partial \mathbf{x}} \Delta \mathbf{v} = -dt \mathbf{H}\mathbf{f} + dt \frac{\partial \mathbf{f}}{\partial \mathbf{x}} \mathbf{v} - \mathbf{H}^T \boldsymbol{\lambda} \mathbf{L}, \quad (\text{S3})$$

where  $\mathbf{M}$  is the mass matrix,  $\mathbf{f}$  holds the different force functions,  $\mathbf{x}$  and  $\mathbf{v}$  are the position and velocity vectors,  $dt$  the discrete time step, and the  $\mathbf{H}$  matrix contains the constraints directions and the Lagrange multiplier. Furthermore, to simulate the pushing effect of the helix, we complemented the simulator described in (58) by applying an external force in the axial direction on the nodes that are in contact with the vessel wall. We assume that the applied force  $F_{hel} = F_{slip}$  (see “Analytical formulation of helix pushing force”).

For the parameter tuning of the device stiffness, we conducted a calibration process using experimental data from the "Reachable workspace" section (see fig. S3A). The length, diameters, and magnetization of the simulated mCR were fixed, whereas the Young's modulus of the body and the tip were tuned by hand to match the bending behavior of the real device (see table S1).

To calibrate the helix force, we replicated the experiment described in the "Helix effectiveness" section and manually increased the helix force factor until the simulated mCR exhibited comparable behavior to the real experiment (see fig. S3B).

A detailed list of the fixed parameters can be found in table S1 of the Supplementary Materials.

### **Segmentation and 3D printing of vasculature**

The 3D segmentation was done with two angiographic X-ray images of two different projection planes. The images were imported in a computer aided design (CAD) software aligned in 3D by using common features in both images and oriented using the fluoroscope angle settings. The vessels were then manually back-projected to reconstruct a full three-dimensional model. The vasculature model was 3D printed using stereolithography (SLA) from the photopolymer resin WaterShed® XC 11122. It was printed with 2 mm wall thickness and a resolution of 0.05mm, followed by a sandblasting and varnish surface finish to improve transparency.

### **In vitro simulation of the in vivo experiments**

The helical microcatheter was navigated in a transparent SLA-printed model. The model is based on a segmentation of the porcine vasculature from the in vivo experiments. The phantom model was placed at the same position with respect to the eMNS coils as were the vessels in the in vivo experiment. The device was imaged under fluoroscopy and navigated from a shielded control room. The model was filled with a solution made of water (70 %), soap (10 %) and a contrast medium (20 %).

**Figures:**

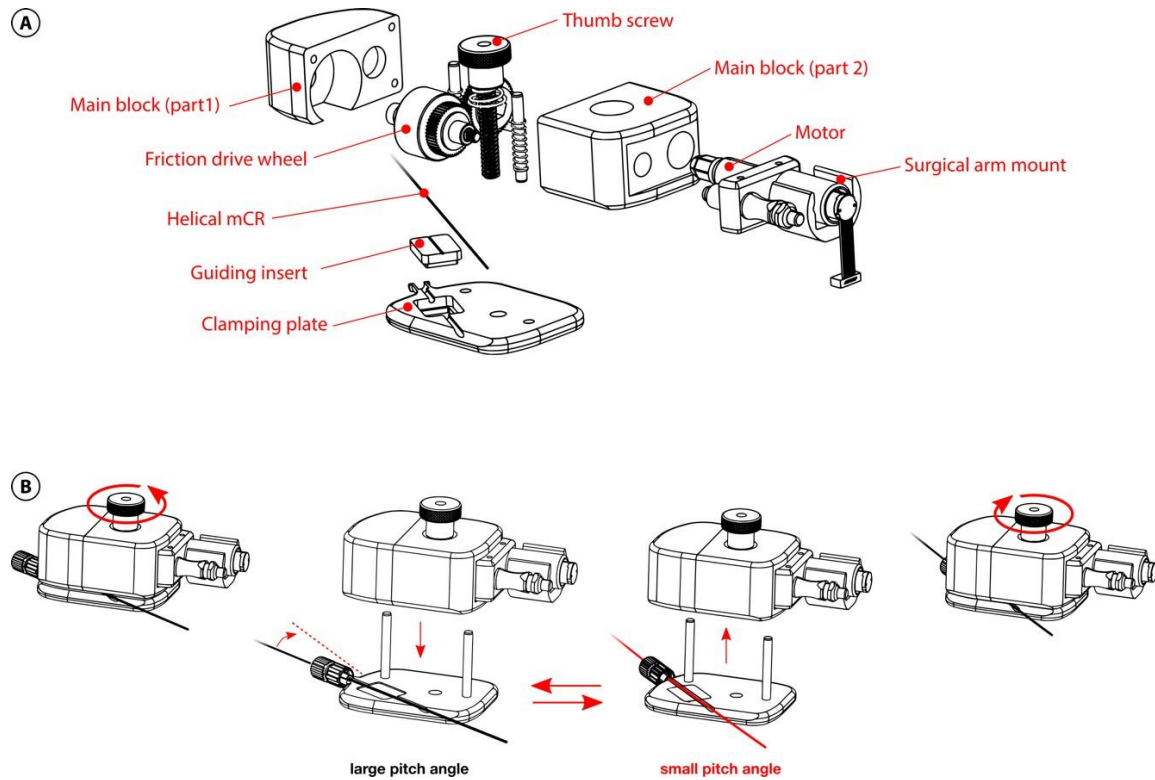


**Fig. S1. Detailed illustration of the advancer unit.** (A) Graphical view of the advancer unit. (B) The angle between the guiding insert and the drive wheel is adjusted by fully unscrewing the thumb screw, replacing the entire clamping plate with the guiding groove by a new plate with different guiding angle, and by retightening the thumb screw.

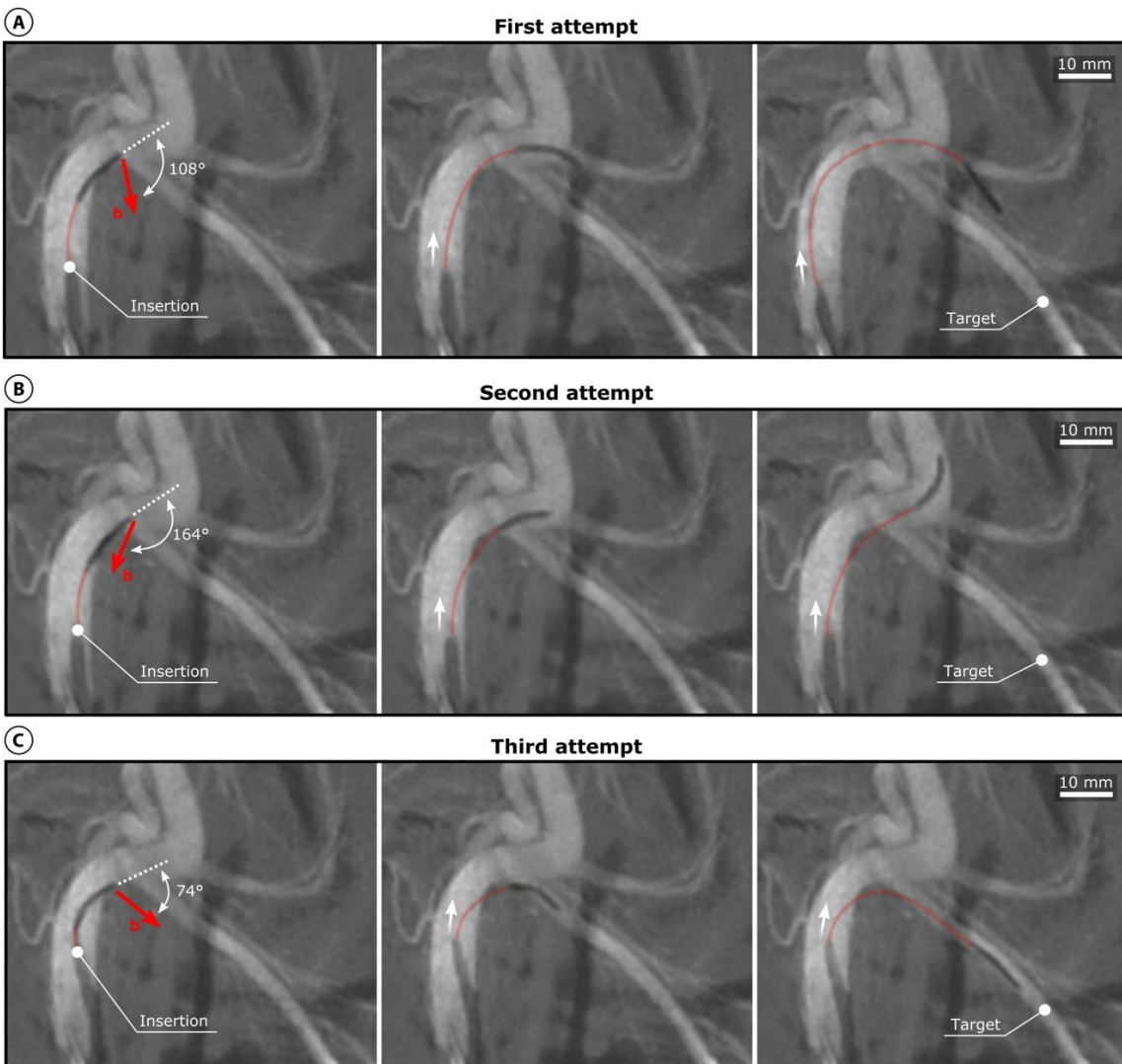


**Fig. S2. Post-interventional analysis of the in vivo navigation.** Three attempts were required to select an artery with a large bifurcation angle. (A), (B) The first two attempts had an excessive offset angle between the magnetic tip and the external magnetic field. The magnetic torque was not sufficient to enter the target artery. (C) Successful navigation with large magnetic torque and an offset angle close to  $90^\circ$ .

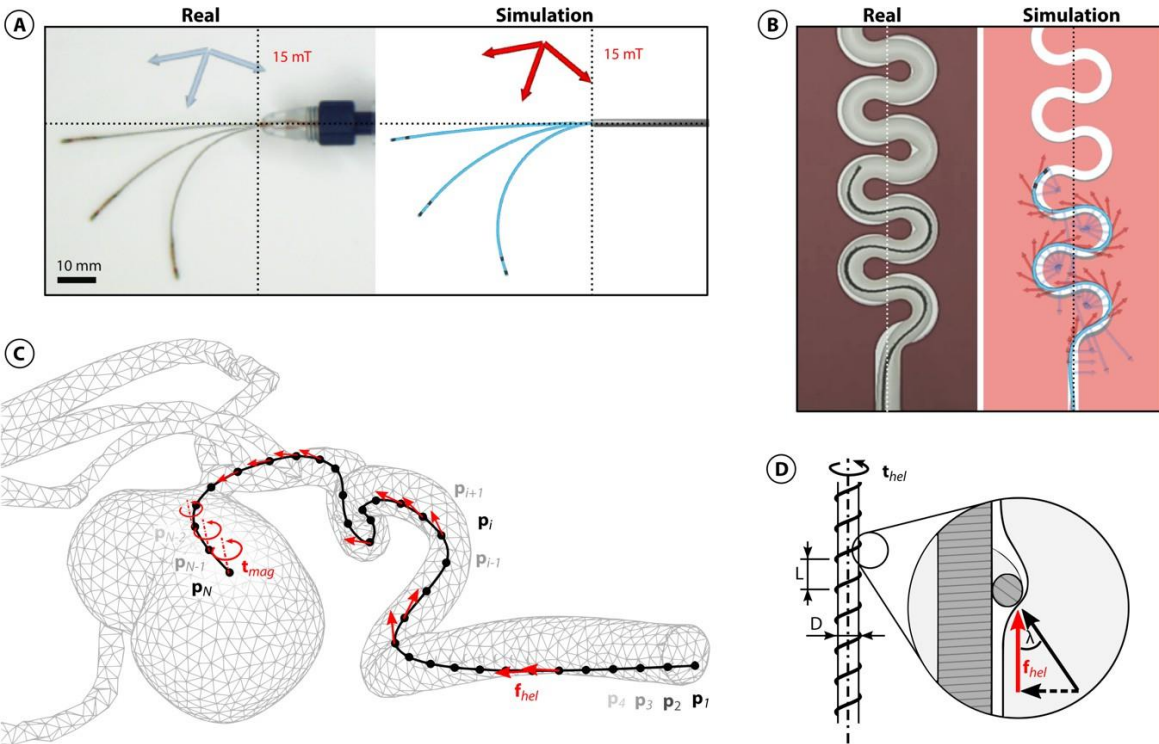


**Fig. S3. Modelling and simulation of the helical magnetic continuum robot.** (A) The parameter tuning of the simulated device stiffness and (B) the helix pushing force  $F_{hel} = \|\mathbf{f}_{hel}\|$  (red arrows). (C) An illustration of the discretized magnetic continuum robot navigating in a discretized vascular model. The helix is pushing the device forward at every point of contact  $\mathbf{p}_i$  and a magnetic torque  $\mathbf{t}_{mag}$  steers the tip of the device. (D) A force analysis of the helix engaging with the vessel wall. The pushing helix pushing force  $\mathbf{f}_{hel}$  is a function of the helix pitch length  $L$ , the mean helix diameter  $D$ , and the engagement angle  $\lambda$ . The engagement angle describes the quality of the engagement. The more the helix engages with the vessel wall, the more torque is translated into pushing force.



**Tables:****Table S1. Parameters of the simulated helical magnetic continuum robot.**

Parameter fixed	Value
Inner diameter body (m)	$0.17 \times 10^{-3}$
Outer diameter body (m)	$0.7 \times 10^{-3}$
Length body (m)	0.2
Elements body	100
Inner diameter magnetic tip (m)	$0.17 \times 10^{-3}$
Outer diameter magnetic tip (m)	$0.7 \times 10^{-3}$
Length magnetic tip (m)	$3 \times 10^{-3}$
Elements magnetic tip	3
Remanence magnetic element (T)	1.45
Friction coefficient	0.01

Parameter calibrated	Value
Young's Modulus body (Pa)	$800 \times 10^6$
Young's Modulus tip (Pa)	$600 \times 10^6$
Helix pushing force per node (N)	$0.15 \times 10^{-3}$